Study of the Two-band Hubbard Model by the Dynamical Mean Field Theory

Tetsuya MUTOU

January, 1997

Study of the Two-band Hubbard Model by the Dynamical Mean Field Theory

Tetsuya MUTOU

A dissertation submitted to the Doctoral Program in Physics,
the University of Tsukuba in partial fulfillment of the
requirements for the degree of Doctor of Philosophy (Science)

January, 1997

Acknowledgements

I would like to express my sincerest gratitude to Prof. Dai S. Hirashima, who introduced me to this field of research, for his guidance, valuable discussions, critical reading of the manuscript, and his continual encouragements. I would like to thank Prof. Satoshi Takada and Prof. Kenn Kubo for useful discussions and their encouragements. I am grateful to Dr. Yoji Ohashi for critical reading of a part of the manuscript. I am also indebted to Prof. Akira Oguri for useful information about the maximum entropy method. I am also thankful to Prof. Masatoshi Imada, Dr. Nobuo Furukawa, Prof. Yoshio Kuramoto, Prof. Atsushi Fujimori, and Dr. Isao H. Inoue for fruitful discussions and useful comments. Many stimulating conversations with the members of the research group at the University of Tsukuba are much acknowledged.

The computation in this work has been done using the facilities of the Super-computer Center, Institute for Solid State Physics, University of Tokyo, and the facilities of the Information Center, University of Tsukuba.

Finally, I thank my parents for mental and financial support, and I also thank Ms. C. Mise for her encouragements.

List of papers submitted for the requirement of the degree

1. "Spectral weight transfer in a doped strongly correlated insulator", Tetsuya Mutou and Dai S. Hirashima: Phys. Rev. **B 54**, 9058-9061 (1996).

2. "Enhancement of the Magnetic Susceptibility of a Periodic Anderson Model", Tetsuya Mutou and Dai S. Hirashima: J. Phys. Soc. Jpn. **65**, 369-371 (1996).

3. "Gap Formation in the Symmetric Periodic Anderson Model in Infinite Dimensions. II", Tetsuya Mutou and Dai S. Hirashima: J. Phys. Soc. Jpn. **64**, 4799-4812 (1995).

4. "Gap Formation in the Symmetric Periodic Anderson Model in Infinite Dimensions", Tetsuya Mutou and Dai S. Hirashima: J. Phys. Soc. Jpn. **63**, 4475-4488 (1994).

5. "Weak-coupling theory of the periodic Anderson model in infinite dimensions", Dai S. Hirashima and Tetsuya Mutou: Physica B **199&200**, 206-208 (1994).

Contents

Chapter 1

General introduction

1.1 Introduction

The discovery of the high-T_c superconducting cuprates [1] has revived the interest in strongly correlated electron systems, which have been studied for a long time in connection with the study of the electronic states in the transition-metal compounds. In the transition-metal compounds, the strong correlation between the $3d$ electrons is essentially important.

On the other hand, in the intensive studies of the high-T_c cuprates, it has been shown that in order to investigate the electronic states the systematic control of the carrier concentration is important, because the occurrence of the superconductivity is sensitive to the carrier concentration. In other transition-metal compounds, the systematic experimental studies have been triggered by the discovery of the high-T_c cuprates. In the experimental studies, the carrier concentration and the relative interaction strength are controlled by the chemical substitution while keeping conducting networks in the transition-metal compounds. For example, in $Ca_{1-x}Sr_xVO_3$ one can systematically control the relative interaction strength by changing the concentration x of Sr.

For the change of the carrier concentration or the relative interaction strength, there is an interesting phenomenon in the strongly correlated electron systems. It is the Mott transition, which is a transition between the metallic phase and the strongly correlated insulating phase. The high-T_c superconductivity occurs near the transition and the property of the itinerant electronic states which are formed on carrier doping has attracted considerable interest. On the other hand, $Ca_{1-x}Sr_xVO_3$ is a metallic compound which is near the transition and the interaction-strength dependence of the electronic states has received attention.

Though there have been various studies of the Mott transition for a long time, the comprehensive understanding of the electronic states on the metallic side of the Mott transition is still lacking, because it is difficult to treat the strong correlation theoretically. Thus, some problems about the electronic states remain unsolved. One of the problems is how the itinerant electronic states emerges in the metallic phase near the transition.

In the thesis, we would like to solve the abovementioned problem by treating suitably the electron correlation, and to clarify the origin of the itinerant electronic states in the metallic side of the Mott transition in the transition-metal compounds. We consider the one-particle-excitation spectral function in order to investigate the electronic states. We can directly obtain the occupied and unoccupied electronic states from the spectral function.

We need to use a method by which we can properly treat the strong electron correlation. In the present study, we use the *dynamical mean field theory* (DMFT), which has been developed recently, and successfully applied to the strongly correlated systems. In the theory, while the spatial fluctuations are neglected, the local quantum fluctuations can be correctly treated.

We also need to use a theoretical model which is suitable to describe the transition-metal compounds. Though the narrow $3d$ band is essential for the strong electron correlation, the anion orbital can become important in the transition-metal compounds. For example, in the high-T_c cuprates, the importance of the O $2p$ orbital was also pointed out, because it was clarified that the doped hole enters in the p orbital. In the thesis, therefore, we explicitly consider the effect of p orbital in the transition-metal compounds by using the two-band Hubbard model.

According to Zaanen, Sawatzky, and Allen, the transition-metal compounds are qualitatively classified into two groups by magnitude of charge-transfer energy: the charge-transfer-type system and the Mott-Hubbard-type system [2]. The high-T_c cuprates belong to the former and $Ca_{1-x}Sr_xVO_3$ to the latter. Using the two-band Hubbard model, we can treat the systems correspond to the both types on an equal footing.

Let us summarize the purpose of the thesis; applying the DMFT to the two-band Hubbard model, we investigate the change of the one-particle-excitation spectral function: (1) the carrier concentration dependence for the charge-transfer-type insulator and (2) the interaction strength dependence for the Mott-Hubbard-type insulator, and clarify how the spectral intensity corresponding the itinerant electronic state emerges in the metallic side of the Mott transition. We also clarify the character of the itinerant electronic states in each case.

This thesis is organized as follows. We first survey the studies of the MIT

in the strongly correlated systems (the Mott transition) in Section 1.2. We focus on the problem why NiO is a non-conductor although it is expected to be metallic in the band theory. We also review the theoretical studies of the Mott transition. There is one of the successful example of the DMFT in the study of the Mott transition. We briefly review the derivation of the DMFT in Chapter 2. One can reduce the lattice problem to an effective impurity problem by the DMFT. In the chapter, we also review the methods to solve the effective impurity problem. In Chapter 3, we discuss the classification of the two types of the transition-metal compounds according to Zaanen, Sawatzky, and Allen. in Chapter 3. We introduce the two-band Hubbard model and show the formulation of the present study in the chapter. The numerical results for the charge-transfer-type system in Chapter 4, and those for the Mott-Hubbard-type system are shown in Chapter 5, respectively. Chapter 6 contains the concluding remarks.

1.2 Mott transition

In the transition-metal compounds, it is well accepted that the strong Coulomb interaction between $3d$ electrons is important. The insulating phase in some transition-metal compounds cannot be explained by the conventional band theory, and it is caused by the strong correlation between electrons. The insulating materials caused by the strong correlation are called Mott insulators, and the transition from a metallic state to an insulating state induced by the strong correlation is called the Mott transition.

We briefly review the historical development in the studies of the Mott transition in this section. First we show the important suggestion for the non-conducting property of NiO by Mott [4, 5, 6] in Section 1.2.1. In the section, we also introduce examples of the perovskite-type transition-metal oxides which attract considerable interest recently. In Section 1.2.2, we review the main theoretical studies of the Mott transition and show a successful example of the application of the DMFT to the strongly correlated systems.

1.2.1 Mott insulator

The electronic states of the transition-metal compounds have been controversial problems. One of the puzzling problems was that NiO is an insulating compound although it was predicted to be metallic from the conventional band theory [3, 4]. Mott discussed the problem in detail and pointed out that the strong Coulomb interaction between $3d$ electrons drives the system into an

insulator [5]. This is why the Mott insulator is so named.

In the transition-metal oxide NiO (Ni^{2+}:$3d^8$, O^{2-}:$2p^6$), the $3d$ orbitals split by a cubic crystal field into sub-orbitals, $d\gamma$ (doubly degenerate) and $d\epsilon$ (triply degenerate). The energy bands consisting of $d\gamma$ orbitals are partially filled in accord with the Hund rule. According to the conventional band theory, then, NiO is expected to be metallic. In reality, NiO is an insulator.

Mott suggested a qualitative explanation of the insulating behavior of NiO [4, 5]. According to his explanation, the insulating property of NiO is caused by the excitation energy required to remove an electron from a certain Ni^{2+} ion (leaving Ni^{3+}) and to put it on another Ni^{2+} ion (forming Ni^{+}). When the increase of the Coulomb energy is larger than the transfer energy of electrons, the excitation energy is positive and the system becomes an insulator.

The mother materials of the high-T_c superconducting cuprates are also the Mott insulators. In La_2CuO_4 (Cu^{2+}:$3d^9$), for example, the $3d$ orbitals split into $d\gamma$ and $d\varepsilon$, and the band consisting of $d\gamma$ orbitals (which further split by a square crystal field) is partially filled. Namely, according to the simple band theory, La_2CuO_4 should be metallic. In spite of the prediction of the band theory, the material shows the insulating behavior of the resistivity [7]. One can dope carriers (holes) into the system by the substitution of Sr^{2+} for La^{3+}. The substitution partially changes the valence of $(CuO_4)^{6-}$ to $(CuO_4)^{4-}$, and carriers are doped into the CuO_2 planes. Since the superconducting phase appears only in the low-density-doping region (e.g. $0.06 \lesssim x \lesssim 0.26$ for $La_{2-x}Sr_xCuO_4$ [8, 7, 9]), it is recognized that it is important to investigate the electronic states near the Mott transition.

1.2.2 Theories of Mott transition

The essence of the Mott transition is the competition between the local electron-electron interaction energy and the kinetic energy of the itinerant electrons. The simplest model that describes the competition is the Hubbard model;

$$\hat{\mathcal{H}}_{\rm Hub} = -t \sum_{<i,j>} (c^\dagger_{i\sigma} c_{j\sigma} + {\rm H.c.}) + U \sum_i c^\dagger_{i\uparrow} c_{i\uparrow} c^\dagger_{i\downarrow} c_{i\downarrow}, \tag{1.1}$$

where we assume only the nearest-neighbor hopping. In eq.(1.1), t is the hopping energy, and U is the on-site Coulomb interaction energy. The theoretical studies of the Mott transition using the Hubbard model have been carried out for a long time.

Here we first review two approaches from the opposite directions, i.e., from the atomic limit and from the metallic limit. We then introduce a study by the DMFT, which interpolates the two approaches.

Approaches from the atomic limit and from the metallic limit

In a series of papers, Hubbard investigated the change in the density of states caused by the interaction. He calculated the one-particle Green's function using decoupling techniques and a CPA(coherent potential approximation)-like approximation [10, 11]. He showed that the density of states splits into two subbands when the ratio U/t becomes greater than a critical value, and consequently the system is turned into an insulator. (Therefore, we refer to the subbands as the upper and lower Hubbard bands.)

As the theory is guided by the principle that it should be correct in the atomic limit $t \to 0$, it is a good approximation in the insulating region. It was pointed out [12], however, that it fails in the metallic region; for example, no well-defined Fermi surface exists even in the metallic phase.

Another approach is taken by Brinkman and Rice [13] on the basis of the Gutzwiller variational wave function [14]. In the approach, the Fermi surface exists in the distribution of occupied states when the system is metallic. Brinkman and Rice showed that both the number of the doubly occupied sites and the discontinuity at the Fermi surface become zero at a critical value of U, U_c.

However, Yokoyama and Shiba showed that the transition does not occur in the correct treatment of the Gutzwiller wave function; the appearance of the transition is an artifact due to the Gutzwiller approximation [15]. This shows that the Gutzwiller wave function is not good enough to describe the Mott transition in finite dimensions.

Mott transition described by DMFT

A result which connects the two approaches from the atomic limit and from the metallic limit was obtained by a method within the DMFT framework [17, 18, 16]. The method is called the iterated perturbation theory (IPT) [19] (see also Chapter 2). In the method, the self-energy calculated by the second-order perturbation with respect to U is shown to become exact in both the weak-coupling limit and the strong-coupling limit. Thus it is expected that the method provides an interpolation scheme between the both limits [16].

In the study, it was shown that the one-particle-excitation spectrum has three remarkable structures; the lower and upper Hubbard bands, and the sharp peak at the Fermi level. In the Mott transition, both the width of the sharp peak in the spectrum and the discontinuity at the Fermi surface in the distribution of occupied states become zero at a critical value $U = U_c$ [18].

The study is one of the successful examples of the application of the DMFT to the strongly correlated systems. We can expect that the DMFT is a useful

method to study the electronic states near the Mott transition. We derive the DMFT in the next chapter.

Chapter 2

Dynamical mean field theory (DMFT)

The idea of the DMFT originated from the analysis of the system in infinite dimensions, where the self-energy of the Green's function becomes local. In the DMFT, the spatial fluctuations are neglected, but the local quantum fluctuations can be fully considered. Namely, while the spatial correlation is treated only as a mean field, the on-site quantum dynamics can be exactly treated. One can reduce a problem of a lattice system to an impurity problem embedded in an effective medium (the dynamical mean field). In Section 2.1, we briefly mention the relation between the local approximation of the self-energy and the DMFT, and derive the DMFT. We review various methods to solve the effective impurity problem within the DMFT framework in Section 2.2.

2.1 DMFT and local approximation of the self-energy

2.1.1 Infinite-dimensional model and local self-energy

In spite of its simple form, the Hubbard model is exactly solved only in one dimension [20]. In two or three dimensions, there are only approximate calculations and numerical simulations for finite-size systems.

Recently, however, an important advance has been made in the infinite-dimensional limit. The infinite-dimensional Hubbard model was first introduced by Metzner and Vollhardt [21]. In order to define a non-trivial model in which the kinetic term and the potential term are of the same order, the

intersite hopping energy t should be scaled as $t \to \tilde{t} \propto 1/\sqrt{z}$, where z is the number of nearest-neighbor sites, namely, the coordination number [21].

One of the remarkable properties of the infinite-dimensional system they found was that the self-energy of the Green's function becomes site-diagonal [21, 22]. The property is shown by simple power counting as follows. One of the standard methods to calculate the Green's function of the system is a perturbation theory with respect to the on-site Coulomb interaction energy U. In general, the Green's function $G_{ij}(\mathrm{i}\omega_n)$ connecting a site i to a site j is expanded by the self-energy $\Sigma_{ij}(\mathrm{i}\omega_n)$;

$$G_{ij}(\mathrm{i}\omega_n) = G^0_{ij}(\mathrm{i}\omega_n) + \sum_{kl} G^0_{ik}(\mathrm{i}\omega_n)\Sigma_{kl}(\mathrm{i}\omega_n)G^0_{lj}(\mathrm{i}\omega_n) + \cdots, \tag{2.1}$$

where $G^0_{ij}(\mathrm{i}\omega_n)$ is the free ($U = 0$) Green's function. (In the above expression, ω_n is the Matsubara frequency defined by $\omega_n = (2n+1)\pi T$, where T is the temperature and n is an integer.) For example, we consider the second order self-energy, $\Sigma^{(2)}_{ij}$, which includes three G^0_{ij}'s. Since t is scaled by $1/\sqrt{z}$, G^0_{ij} involves a factor $1/\sqrt{z}$ even for the nearest sites $< i, j >$. Hence, the second order self-energy, $\Sigma^{(2)}_{ij}$, between the nearest sites $< i, j >$ involves a factor $(1/\sqrt{z})^3$. On the other hand, the summation of the nearest neighbor sites j brings in a factor of order z. Thus, we obtain at least an overall factor of $1/\sqrt{z}$ for the non-local second order self-energy, $\Sigma^{(2)}_{ij}$. One can apply a similar argument to the higher-order terms, and finds that only the local contribution ($i = j$) survives in the infinite-coordination number limit (i.e., the infinite-dimensional limit).

As a simple consequence of the locality of the self-energy, Müller-Hartmann showed that, in the single-band Hubbard model, the density of states at the Fermi level is invariant for any strength of U as long as the system is the Fermi liquid state [23] (see Appendix E).

Using the site-diagonal self-energy, the local Green's function can be expressed using the energy integral as

$$\begin{aligned} G(\mathrm{i}\omega_n) &= \frac{1}{N}\sum_{\boldsymbol{k}} \frac{1}{(G^0_{\boldsymbol{k}}(\mathrm{i}\omega_n))^{-1} - \Sigma(\mathrm{i}\omega_n)}, \\ &= \int \mathrm{d}\epsilon \frac{\rho_0(\epsilon)}{\mathrm{i}\omega_n + \mu - \epsilon - \Sigma(\mathrm{i}\omega_n)}, \end{aligned} \tag{2.2}$$

where $\rho_0(\epsilon)$ is the density of states defined by

$$\rho_0(\epsilon) = \frac{1}{N}\sum_{\boldsymbol{k}} \delta(\epsilon - \varepsilon(\boldsymbol{k})). \tag{2.3}$$

In the expression, $\varepsilon(\boldsymbol{k})$ is the Fourier transformation of the hopping energy in (1.1).

2.1.2 Effective impurity problem

Making full use of the locality of the self-energy, one can construct an exact "mean-field-type" theory of the lattice problem [16]. Let us explain one of the procedures to obtain the "mean field" description [24, 25]. Since the self-energy is local in eq. (2.1), the local Green's function $G_{ii}(\mathrm{i}\omega_n)$ for a certain site i can be rearranged to contain explicitly only the i-site "bare" Green's function $\mathcal{G}_{ii}(\mathrm{i}\omega_n)$, in which effects of the interaction at all the sites *except* the site i are included. Namely, $G_{ii}(\mathrm{i}\omega_n)$ is expressed as;

$$\begin{aligned} G_{ii}(\mathrm{i}\omega_n) &= \mathcal{G}_{ii}(\mathrm{i}\omega_n) + \mathcal{G}_{ii}(\mathrm{i}\omega_n)\Sigma(\mathrm{i}\omega_n)\mathcal{G}_{ii}(\mathrm{i}\omega_n) \\ &+ \mathcal{G}_{ii}(\mathrm{i}\omega_n)\Sigma(\mathrm{i}\omega_n)\mathcal{G}_{ii}(\mathrm{i}\omega_n)\Sigma(\mathrm{i}\omega_n)\mathcal{G}_{ii}(\mathrm{i}\omega_n) + \cdots . \end{aligned} \tag{2.4}$$

The formal Dyson equation of $\mathcal{G}_{ii}$ is

$$\begin{aligned} \mathcal{G}_{ii}(\mathrm{i}\omega_n) &= G^0_{ii}(\mathrm{i}\omega_n) + \sum_{j\neq i} G^0_{ij}(\mathrm{i}\omega_n)\Sigma(\mathrm{i}\omega_n)\mathcal{G}_{ji}(\mathrm{i}\omega_n) \\ &= G^0_{ii}(\mathrm{i}\omega_n) + \sum_{j} G^0_{ij}(\mathrm{i}\omega_n)\Sigma(\mathrm{i}\omega_n)\mathcal{G}_{ji}(\mathrm{i}\omega_n) - G^0_{ii}\Sigma(\mathrm{i}\omega_n)\mathcal{G}_{ii}(\mathrm{i}\omega_n) \end{aligned} \tag{2.5}$$

By the Fourier transformation for the both sides of eq.(2.5), one obtains the expression in the wave-number space,

$$\mathcal{G}_{\boldsymbol{k}}(\mathrm{i}\omega_n) = G^0_{\boldsymbol{k}}(\mathrm{i}\omega_n) + G^0_{\boldsymbol{k}}(\mathrm{i}\omega_n)\Sigma(\mathrm{i}\omega_n)(\mathcal{G}_{\boldsymbol{k}}(\mathrm{i}\omega_n) - G^0_{ii}(\mathrm{i}\omega_n)). \tag{2.6}$$

By solving eq.(2.6) for $\mathcal{G}_{\boldsymbol{k}}$ and summing the both sides on $\boldsymbol{k}$, $\mathcal{G}_{ii}$ is expressed by

$$\mathcal{G}_{ii}(\mathrm{i}\omega_n) = (1 - \Sigma(\mathrm{i}\omega_n)\mathcal{G}_{ii}(\mathrm{i}\omega_n))G_{ii}(\mathrm{i}\omega_n)), \tag{2.7}$$

where we have used the $\boldsymbol{k}$-summation expression of the local Green's function (2.2). From eq.(2.7), one can obtain the final expression of the local Green's function $G(\mathrm{i}\omega_n)$ using $\mathcal{G}$ as

$$G^{-1}(\mathrm{i}\omega_n) = \mathcal{G}^{-1}(\mathrm{i}\omega_n) - \Sigma(\mathrm{i}\omega_n), \tag{2.8}$$

where we omit the site index by assuming the translational invariance.

On the other hand, one can regard the expression (2.8) as the Dyson equation of the impurity model in which the bare Green's function is given by $\mathcal{G}$. In fact, one can obtain the effective action of an impurity problem embedded in

an effective medium which is described using $\mathcal{G}$. The effective action is derived in the infinite-dimensional limit (see Appendix A):

$$\mathcal{S}_{\text{eff}} = -\int_0^\beta \int_0^\beta \mathrm{d}\tau \mathrm{d}\tau' \sum_\sigma \bar{\psi}_{o\sigma}(\tau)\mathcal{G}^{-1}(\tau-\tau')\psi_{o\sigma}(\tau') + U\int_0^\beta \mathrm{d}\tau \bar{\psi}_{o\uparrow}(\tau)\psi_{o\uparrow}(\tau)\bar{\psi}_{o\downarrow}(\tau)\psi_{o\downarrow}(\tau), \tag{2.9}$$

where $\bar{\psi}_{o\sigma}$ ($\psi_{o\sigma}$) is the Grassmann variable corresponding to the fermion creation (annihilation) operator at a certain site o. There is on-site Coulomb interaction U between the fermions at the site o. The effective action can be interpreted as an action of a system in which $\mathcal{G}$ is a *bare* impurity Green's function and the on-site repulsion exists only at the o-site. Since $\mathcal{G}$ includes the information of the other sites, it plays the role of a "mean field".

The similar simplicity also occurs in the classical spin system. In the classical spin system, it is known that the description using the usual mean field, in which all fluctuations are neglected, becomes exact in the infinite-dimensional (infinite-range-coupling) limit. In the present "mean field" theory, however, one takes full account of local quantum fluctuations. Therefore the approach is called the *dynamical mean field theory* (DMFT) [16].

In the DMFT framework, there are three relations (eq.(2.2), (2.8), and (2.9)), and three unknown quantities ($G(\mathrm{i}\omega_n)$, $\mathcal{G}(\mathrm{i}\omega_n)$, and $\Sigma(\mathrm{i}\omega_n)$). Therefore, if one can solve the effective impurity problem (2.9), the solution of the lattice problem can be obtained exactly by solving the self-consistent equations.

Before proceeding we give a remark. The DMFT can be derived without taking the infinite-dimensional limit, if only one assumes the self-energy to be local. Thus, one can regard the DMFT as an approximate method in finite dimensions. In the thesis, we apply the DMFT to the present study regarding it as the approximate method in which one neglects the $\boldsymbol{k}$-dependence of the self-energy. The approximation was shown to be excellent in three dimensions; the result of the second-order correlation energy with respect to U for the Hubbard model on the cubic lattice is well approximated by that of the infinite-dimensional model [21].

2.2 Methods to solve the effective impurity problem

The on-site quantum problem (the effective impurity problem) in the DMFT framework still remains a many-body problem, and one has to solve the problem by an appropriate method. Several methods to solve the impurity problem were developed in the studies of a magnetic impurity in a metal: the numer-

ical renormalization group method [26], the perturbation theory [27], and the quantum Monte Carlo method [28], and so on. These various methods are also successfully applied to the effective impurity problem in the DMFT [16]. Let us briefly review these applications. Here, we mention those examples focusing on the applications to the single-band Hubbard model.

Iterated perturbation theory

The method in which the self-energy is calculated from $\mathcal{G}$ by the second-order perturbation theory was applied by Georges *et al.* [17] and Zhang *et al.* [18]. (It is the iterated perturbation theory (IPT) mentioned in Section 1.2.2.) This corresponds to the method used by Yosida and Yamada for the impurity Anderson model [27]. It is shown that the (second-order) self-energy obtained by this method becomes exact in both the weak-coupling limit ($U/t \to 0$) and the strong-coupling limit ($U/t \to \infty$) in the particle-hole symmetric case. Thus, the IPT approximation is expected to provide a correct result even in the strong-coupling regime in the special case [18]. In the case, the IPT approximation for the self-energy automatically satisfies the conservation law of the number of particles. However, one cannot determine the self-energy by which the conservation law is satisfied in the particle-hole asymmetric case any more. (Recently, the modified IPT, which one can apply to the particle-hole asymmetric case, was developed by Kajueter *et al.* [29].)

Numerical renormalization group method

The numerical renormalization group method was applied to solve the effective impurity problem by Sakai and Kuramoto [30]. This is a powerful method to study the low-temperature or low-energy limit case. One can obtain the wave functions and the dynamical response functions by the method. Sakai and Kuramoto applied the method to the half-filled case and calculated the density of states of the system. However, it is difficult to extend the method to finite temperatures.

Exact diagonalization method

Caffarel and Krauth presented a method using the exact diagonalization of an impurity Anderson model with a finite number of sites [31]. In the method, one approximates $\mathcal{G}(\mathrm{i}\omega_n)$ in the DMFT with the bare impurity Green's function of a finite-size cluster of an impurity Anderson model; $\mathcal{G}$ is fitted using the finite parameters of the impurity Anderson model. After fitting, one diagonalizes the cluster of the impurity Anderson model, and calculates the impurity Green's

function using the wave functions of the cluster. The local Green's function $G(\mathrm{i}\omega_n)$ of the original lattice corresponds to the impurity Green's function in the DMFT. Thus, one can determine the final $G(\mathrm{i}\omega_n)$ self-consistently by above procedure together with eqs. (2.2) and (2.8). One can obtain the information about the wave functions of the original lattice problem using this method. However, at finite temperatures, one can calculate the Green's function only for a small cluster. (For a very large cluster, one can not calculate it even at absolute zero.)

Quantum Monte Carlo method

The Hirsch-Fye algorithm of the quantum Monte Carlo method [28] was used to calculate various physical properties of the single-band Hubbard model [24, 25, 32, 33, 34, 35]. Though the method is not suitable to study the properties at low temperatures, it is powerful to investigate the system at finite temperatures. By using the method, the Mott transition was discussed at half-filling [24, 25, 32, 33]. Besides, Jarrell *et al.* discussed the antiferromagnetic instability near the Mott transition and obtained the spectral functions of the one-particle excitation and the spin excitation by this method together with the maximum entropy method [24, 25]. Saso and his collaborators calculated the magnetization curve [34], and obtained the one-particle- excitation spectral functions under a finite magnetic field by the maximum entropy method [35].

We study one-particle-excitation spectral functions in the wide region from the low energy to the high energy. In the thesis, we use the Hirsch-Fye algorithm of the quantum Monte Carlo method together with the maximum entropy method.

Chapter 3

Model and Formulation

In this chapter, we introduce the model which we use in the thesis, and show the formulation of the calculation in the present study.

We first briefly review the Zaanen-Sawatzky-Allen's diagram [2], a qualitative classification for the transition-metal compounds, in Section 3.1. We introduce the two-band Hubbard model in Section 3.2. In Section 3.3, we show the procedure to calculate the one-particle-excitation spectral functions.

3.1 Transition-metal compounds and Zaanen-Sawatzky-Allen diagram

After the studies by Mott [4, 5, 6] and Hubbard [11], it had been vaguely believed that the insulating phase of transition-metal compounds was caused by the Coulomb interaction energy U of $3d$ electrons and the magnitude of the gap is roughly given by U. (Such insulating materials are called Mott-Hubbard insulators.)

However, for NiO, Fujimori *et al.* carried out the local-cluster (NiO_6^{10-}) calculation, and pointed out that in order to interpret the photoemission (electron-removal) spectrum of NiO it is needed to take account of not only the $3d$ band but also the ligand band [36]. In the photoemission and inverse-photoemission spectroscopic experiments, Sawatzky *et al.* observed the excitation gap, and concluded that the gap is not solely determined by the Ni $3d$ Coulomb interaction (or the gap was not proportional to the Coulomb interaction), namely NiO was not a Mott-Hubbard insulator in the narrow sense [37].

Following these studies, Zaanen, Sawatzky and Allen (ZSA) presented a phase diagram in which the transition-metal compounds were qualitatively

classified [2]. They calculated the energy gap $E_{\rm gap}$ using the impurity Anderson model in which the transition-metal ion is treated as an impurity.

In the Mott-Hubbard theory it is assumed that the lowest charge excitation is caused by the type $d_i^n d_j^n \rightarrow d_i^{n-1} d_j^{n+1}$, where i and j label sites of the transition-metal ions and n labels the d-orbital occupation. On the other hand, in Ref.[2], ZSA pointed out that there is another type of the charge excitation. It is the charge-transfer-type excitation, $d_i^n \rightarrow d_i^{n+1}\underline{L}$, where $\underline{L}$ denotes a hole in the anion valence band. The charge-fluctuation energy associated with this process is denoted by Δ (Fig. 3.1) [2].

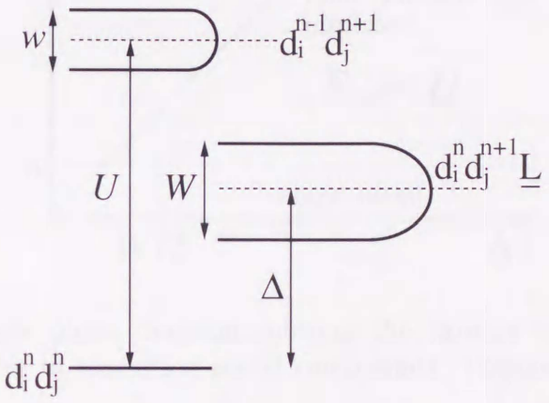

Figure 3.1: Total-energy-level diagram corresponding to an ionic ground state and excitations [2].

In ZSA's calculation, there are four parameters; the charge-transfer energy Δ, the Coulomb interaction between $3d$-electrons U, the anion valence band width W, and the hybridization between a $3d$-electron and anion valence band t. All parameters are scaled by t. [1] For a fixed W, free parameters are Δ and U. The Mott-Hubbard insulators are in the region $\Delta > U$ and the charge-transfer insulators are in $U > \Delta$ [2] (Fig. 3.2). They are distinguished by the lowest-charge-excitation energy corresponding to $E_{\rm gap}$.

Since the electronegativity of the transition metals tends to increase as the atomic number increases, Δ is expected to be small in Co, Ni, and Cu. Thus it is expected that the insulating compounds of the light transition metals (Ti and V) are the Mott-Hubbard insulators and those of the heavy transition metals (Co, Ni, and Cu) are the charge-transfer insulators. In fact, it was

[1] In Fig. 3.1, w denotes the d-band width, which is neglected in the impurity Anderson model.

pointed out that mother materials of the high-T_c cuprates are charge-transfer insulators (see Section 4.1) [42, 43, 44, 45].

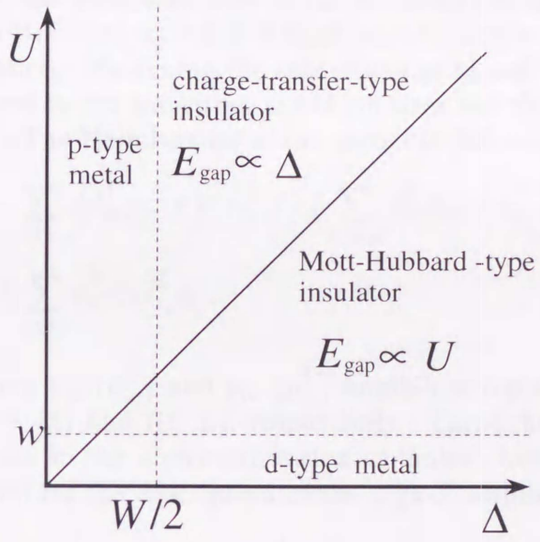

Figure 3.2: Simple phase diagram showing the various types of insulating and metallic states in transition-metal compounds. (Zaanen-Sawatzky-Allen diagram [2].)

In the thesis, we study both the charge-transfer-type system and the Mott-Hubbard-type system. We investigate the carrier concentration dependence of the one-particle-excitation spectral function in the former, and the effect of p orbitals in the latter. Thus, we need to consider the degree of freedom of p orbitals, and should use a multi-band model which includes p orbitals. Let us introduce a simple multi-band model, the two-band Hubbard model in the next section.

3.2 Two-band Hubbard model

One of the standard models to study the strongly correlated systems is the Hubbard model. In the model, the anion p orbital is neglected simply. Hereafter we refer to the model as the *single-band* Hubbard model. Since we investigate the effect of the p orbital, the single-band Hubbard model is not sufficient.

In the thesis, we consider the two-band Hubbard model. The model has two atoms (sites) per unit cell, i.e., the lattice structure is different from the

perovskite-type structure. However, we believe that the two-band Hubbard model is sufficient to study the effect of the anion orbital as long as we do not treat the effects of the band structure or the symmetry of the wave functions.

The two-band Hubbard model is defined on a bipartite lattice which consists of two sublattices. We denote the sublattices as M and L. The sublattices M and L correspond to the transition-metal ion sites and the ligand anion (O) sites, respectively. The Hamiltonian of the model is defined as follows;

$$\begin{aligned}\hat{\mathcal{H}} &= t \sum_{<i,l>,\sigma} (d^{\dagger}_{i\sigma} p_{l\sigma} + \text{H.c.}) + \varepsilon_d \sum_{i\in\text{M},\sigma} d^{\dagger}_{i\sigma} d_{i\sigma} + \varepsilon_p \sum_{l\in\text{L},\sigma} p^{\dagger}_{l\sigma} p_{l\sigma} \\ &+ U_d \sum_{i\in\text{M}} d^{\dagger}_{i\uparrow} d_{i\uparrow} d^{\dagger}_{i\downarrow} d_{i\downarrow}, \end{aligned} \tag{3.1}$$

where the operators $d_{i\sigma}$ ($d^{\dagger}_{i\sigma}$) and $p_{l\sigma}$ ($p^{\dagger}_{l\sigma}$) annihilate (create) fermions with spin σ on sites $i(\in \text{M})$ and $l(\in \text{L})$, respectively. Throughout the thesis, we refer to the fermions in the above expression as 'holes', because the hole representation is useful for the description of the high-T_c cuprates.

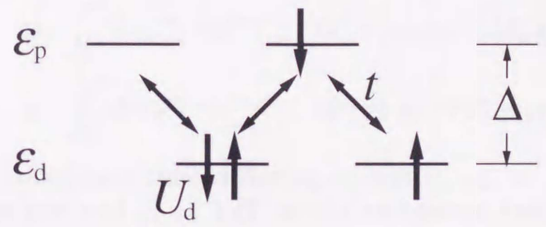

Figure 3.3: Schematic representation of the two-band Hubbard model.

The transfer energy is expressed by t which is defined between the nearest two sites on the M sublattice and the L sublattice. The on-site Coulomb interaction energy on the M site is expressed by U_d. The charge-transfer energy Δ is defined by $\Delta \equiv \varepsilon_p - \varepsilon_d$ where $\varepsilon_{d(p)}$ is the $d(p)$-orbital energy. We set the d-orbital energy to be lower than the p-orbital energy, i.e., $\Delta > 0$. Schematic representation of the two-band Hubbard model is shown in Fig. 3.3.

3.3 Formulation

We show a set of equations of the Green's functions in the self-consistent procedure of the two-band Hubbard model in Sec. 3.3.1. In the procedure, we calculate the imaginary-time local Green's function by the Hirsch-Fye algorithm of the quantum Monte Carlo method (Appendix B.1), and obtain the

spectrum from the imaginary-time local Green's function by the maximum entropy method (Appendix B.2).

In Section 3.3.2, a method of the calculation of the one-particle-excitation spectral function by the single cluster of the two-band Hubbard model is shown. We will compare the one-particle-excitation spectral functions obtained by the quantum Monte Carlo method and the maximum entropy method with those by the single-cluster calculation in Section 4.2 and 5.2.

3.3.1 Self-consistent equations in DMFT

We mainly calculate the d (p)-component of the spectral function $\rho^{d(p)}(\omega)$,

$$\rho^{d(p)}(\omega) = -\frac{1}{\pi}\mathrm{Im}G^{d(p)}(\omega + \mathrm{i}\delta)|_{\delta\to 0+}, \tag{3.2}$$

where $G^{d(p)}(\omega + \mathrm{i}\delta)$ is the $d(p)$-component of the retarded Green's function. The $d(p)$-component of the local Matsubara Green's function is defined as the Fourier transformation of the imaginary-time local Green's function $G^{d(p)}(\tau)$;

$$G^d(\mathrm{i}\omega_n) \equiv \int_0^\beta \mathrm{d}\tau G^d(\tau)e^{\mathrm{i}\omega_n\tau}, \quad G^d(\tau) \equiv -\langle T_\tau[d_{i\sigma}(\tau)d^\dagger_{i\sigma}(0)]\rangle, \tag{3.3}$$

$$G^p(\mathrm{i}\omega_n) \equiv \int_0^\beta \mathrm{d}\tau G^p(\tau)e^{\mathrm{i}\omega_n\tau}, \quad G^p(\tau) \equiv -\langle T_\tau[p_{l\sigma}(\tau)p^\dagger_{l\sigma}(0)]\rangle, \tag{3.4}$$

where T_τ is the imaginary-time ordering operator, $\omega_n = (2n+1)\pi/\beta$ is the Matsubara frequency and $\beta = 1/T$ is the reciprocal temperature (here we set the Boltzmann constant $k_\mathrm{B} = 1$). Since we assume a paramagnetic phase of the system, the spin indices of the Green's functions are omitted. In the above expression, the expectation values are calculated by the grand canonical partition function $\Xi \equiv \mathrm{Tr}e^{-\beta(\hat{\mathcal{H}}-\mu\hat{N})}$ where μ is the chemical potential and $\hat{N}$ is a number operator of the d- and p- holes; $\hat{N} \equiv \sum_{i,\sigma} d^\dagger_{i\sigma}d_{i\sigma} + \sum_{l,\sigma} p^\dagger_{l\sigma}p_{l\sigma}$.

By using the self-energy $\Sigma(\mathrm{i}\omega_n)$ of the d-hole, the local Matsubara Green's functions are expressed as follows;

$$\begin{aligned} G^d(\mathrm{i}\omega_n) &= \int \mathrm{d}\nu\rho_0(\nu)\frac{\mathrm{i}\omega_n + \mu - \varepsilon_p}{(\mathrm{i}\omega_n + \mu - \varepsilon_d - \Sigma(\mathrm{i}\omega_n))(\mathrm{i}\omega_n + \mu - \varepsilon_p) - \nu^2}, \\ G^p(\mathrm{i}\omega_n) &= \int \mathrm{d}\nu\rho_0(\nu)\frac{\mathrm{i}\omega_n + \mu - \varepsilon_d - \Sigma(\mathrm{i}\omega_n)}{(\mathrm{i}\omega_n + \mu - \varepsilon_d - \Sigma(\mathrm{i}\omega_n))(\mathrm{i}\omega_n + \mu - \varepsilon_p) - \nu^2}. \end{aligned} \tag{3.5}$$

In eq.(3.5), $\rho_0(\nu)$ is the density of states in the case of $U_d = 0$ and $\Delta = 0$,

$$\rho_0(\nu) = \frac{1}{N_\mathrm{L}}\sum_{\boldsymbol{k}} \delta(\nu - \varepsilon(\boldsymbol{k})), \tag{3.6}$$

where $\varepsilon(\boldsymbol{k})$ is the Fourier transformation of the hopping energy in (3.1), and $N_{\rm L}$ is the number of sites. Only $\rho_0(\nu)$ has the information of the lattice structure in the DMFT. In the present study, we assume a semi-circular density of state;

$$\rho_0(\nu) = \begin{cases} (2\pi t)^{-1}\sqrt{4-(\nu/t)^2} & (\text{for } |\nu| \le 2t) \\ 0 & (\text{otherwise}). \end{cases} \tag{3.7}$$

The merits of using the semi-circular density of states are that (1) we can precisely define a gap in the spectral functions and (2) we can calculate the integral for ν in eq.(3.5) analytically.

The d-component ($\rho_0^d(\omega)$) and the p-component ($\rho_0^p(\omega)$) of the density of states for $U_d = 0$ are expressed as follows [38];

$$\rho_0^{d(p)}(\omega) = \begin{cases} \sqrt{\dfrac{\omega-\varepsilon_{p(d)}}{\omega-\varepsilon_{d(p)}}}\rho_0\left(\sqrt{(\omega-\varepsilon_p)(\omega-\varepsilon_d)}\right) & (\text{for } 0 \le (\omega-\varepsilon_p)(\omega-\varepsilon_d) \le 4t^2), \\ 0 & (\text{otherwise}). \end{cases} \tag{3.8}$$

We show the structures of them in Fig. 3.4. In Fig.3.4, Γ is given by $(\sqrt{\Delta^2+16t^2}-\Delta)/2$ from eq.(3.8).

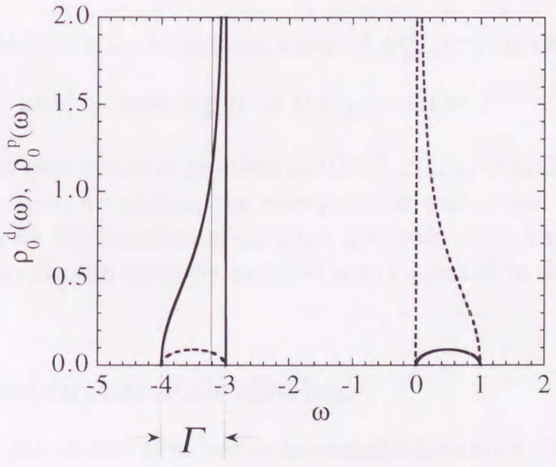

Figure 3.4: Spectral functions for $U_d = 0$, $\Delta = 3$, and $n_{\rm tot} = 1$; solid and broken lines denote d-component and p-component, respectively. The vertical thin line show the position of the chemical potential.

In the DMFT, we introduce the Green's function $\mathcal{G}(i\omega_n)$ which has the information about the effective medium excluding the "impurity" site (see

Chapter 2). We can express the d-component of the local Green's function by using $\mathcal{G}$;

$$G^d(\mathrm{i}\omega_n)^{-1} = \mathcal{G}(\mathrm{i}\omega_n)^{-1} - \Sigma(\mathrm{i}\omega_n). \tag{3.9}$$

After carrying out the integral in (3.5) analytically, we have a set of the equations by eliminating $\Sigma(\mathrm{i}\omega_n)$ from (3.5) and (3.9) as follows; [38]

$$\begin{aligned} \mathcal{G}(\mathrm{i}\omega_n)^{-1} &= \mathrm{i}\omega_n + \mu - \varepsilon_d - t^2 G^p(\mathrm{i}\omega_n), \\ G^p(\mathrm{i}\omega_n)^{-1} &= \mathrm{i}\omega_n + \mu - \varepsilon_p - t^2 G^d(\mathrm{i}\omega_n). \end{aligned} \tag{3.10}$$

If we calculate G^d from $\mathcal{G}$, we can complete the self-consistent procedure in the DMFT. We use the Hirsch-Fye algorithm of the quantum Monte Carlo method (see Appendix B.1) to calculate G^d from $\mathcal{G}$.

We explain the procedure of the Hirsch-Fye algorithm within the DMFT as follows. For an appropriate initial $G^d(\mathrm{i}\omega_n)$,

1. $\mathcal{G}(\mathrm{i}\omega_n)$ is obtained from $G^d(\mathrm{i}\omega_n)$ (through $G^p(\mathrm{i}\omega_n)$) using eqs.(3.10);
2. $\mathcal{G}(\tau_l)$, the inverse Fourier transformation of $\mathcal{G}(\mathrm{i}\omega_n)$, is calculated;
3. the new Green's function $G^d_{\mathrm{new}}(\tau_l)$ is obtained by the Hirsch-Fye algorithm from $\mathcal{G}(\tau_l)$;
4. $G^d_{\mathrm{new}}(\mathrm{i}\omega_n)$, the Fourier transformation of $G^d_{\mathrm{new}}(\tau_l)$, is calculated; and
5. $G^d_{\mathrm{new}}(\mathrm{i}\omega_n)$ is used as new input of the procedure 1.

The self-consistent procedure is iterated until $G^d_{\mathrm{new}}(\mathrm{i}\omega_n)$ coincides with $G^d(\mathrm{i}\omega_n)$. After the convergence, we obtain the one-particle-excitation spectral function $\rho^d(\omega)$ from $G^d(\tau_l)$ by the maximum entropy method. The formulation and the reliability of the maximum entropy method are discussed in detail in Appendix B.2.

3.3.2 Single-cluster calculation

The Green's function in the spectral representation cannot be obtained by the quantum Monte Carlo method and the maximum entropy method. Namely, we cannot directly obtain the initial and final electronic states of the one-particle excitations from the spectral functions calculated by the methods. In order to analyze the spectral functions obtained by the quantum Monte Carlo method and the maximum entropy method, we also carry out another type of the calculation by which we can obtain the initial and final states of the one-particle excitations.

We calculate the d-component of the spectral function using a cluster consisting of one "transition metal" site and z "O" sites. Since electrons are localized in the insulating states, the translational invariance, which is neglected in this single-cluster calculations, is not so essentially important as in metallic states. Thus it is expected that the single-cluster calculations give reliable results for insulating states. The calculation by using a single cluster have been successfully applied to the analysis of the photoemission spectra of the insulating transition-metal compounds [36] and of the undoped high-T_c cuprates [39, 40].

The Hamiltonian of the single cluster is defined by

$$\begin{aligned} \mathcal{H}_{\rm C} &= -\frac{t}{\sqrt{z}}\sum_{l=1}^{z}\sum_{\sigma}(d_\sigma^\dagger p_{l\sigma} + {\rm H.c.}) + \varepsilon_d\sum_{\sigma} d_\sigma^\dagger d_\sigma \\ &+ \varepsilon_p\sum_{l=1}^{z}\sum_{\sigma} p_{l\sigma}^\dagger p_{l\sigma} + U d_\uparrow^\dagger d_\uparrow d_\downarrow^\dagger d_\downarrow . \end{aligned} \tag{3.11}$$

We solve the Schrödinger equation for the cluster Hamiltonian (3.11),

$$\mathcal{H}_{\rm C}|\Psi_m^{(n)}\rangle = E_m^{(n)}|\Psi_m^{(n)}\rangle, \tag{3.12}$$

where $|\Psi_m^{(n)}\rangle$ is the mth excited n-particle eigenstate, and $E_m^{(n)}$ is the corresponding eigenvalue of the cluster. The d-hole spectral function $\rho^d(\omega)$ at $T = 0$ can be calculated by

$$\begin{aligned} \rho_\sigma^d(\omega) &= \frac{1}{2}\sum_{\sigma'}[\sum_m |\langle\Psi_m^{(2)}|d_\sigma^\dagger|\Psi_{0\sigma'}^{(1)}\rangle|^2\delta(\omega - (E_m^{(2)} - E_0^{(1)})) \\ &+ |\langle\Psi^{(0)}|d_\sigma|\Psi_{0\sigma'}^{(1)}\rangle|^2\delta(\omega - E_0^{(1)})], \end{aligned} \tag{3.13}$$

where $|\Psi^{(0)}\rangle$ is the vacuum state. (The one-particle ground states $\Psi_{0\sigma'}^{(1)}$ ($\sigma' = \uparrow, \downarrow$) are doubly degenerate.) The first term in the square brackets represents the hole-addition (or photoemission) spectrum and the second term the hole-removal (or inverse photoemission) spectrum.

Chapter 4

Charge-transfer-type systems

In this chapter, we study the charge-transfer-type systems, in which the $3d$ Coulomb interaction energy U_d is larger than the charge-transfer energy Δ. The high-T_c superconducting cuprate is a typical charge-transfer-type system. One of the important problems is how the itinerant states are formed when the carriers are introduced into the insulating mother material. In order to solve the problem, we study the doping dependence of the one-particle-excitation spectral functions in the two-band Hubbard model.

In Section 4.1, we briefly review the results of the high-energy spectroscopic experiments, and other theoretical studies which treated the spectral functions. Then we show the purposes of the present study. The numerical results are shown in Section 4.2; we show the one-particle-excitation spectral functions in the insulating phase and the carrier number dependence of them in the metallic phase. Finally, we give a summary and discussion in Section 4.3.

4.1 Introduction

In the high-T_c cuprates, a lot of experimental studies have been carried out to clarify the character of the itinerant electronic states. The high-energy spectroscopy is one of the important methods to investigate the electronic states, because one can directly obtain the occupied or unoccupied electronic states from the transition probability of the one-particle excitation. It has indeed revealed [41] that (1) the doped carriers enter O p-orbitals rather than Cu d-orbitals [42, 43, 44, 45]; and that (2) the d-p hybridization between the O p- and Cu d-orbitals is strong [40].

However a comprehensive understanding of the formation of the itinerant electronic states on carrier doping is still lacking. For the doped system the

various models were suggested [46]: for example, (i) the doped charge-transfer-type insulator model where the chemical potential simply shifts as in a rigid-band picture, (ii) the impurity-band model where a narrow impurity band is formed within the charge-transfer gap, and (iii) the filled-gap model where the charge-transfer gap is simply filled up.

In the high-energy spectroscopic experiments it was shown that when the carriers are doped into the system the spectral weight transfers from the high-energy region to the low-energy region [47, 48], and the change of the spectral functions is different from a simple rigid-band picture (i); in the rigid-band picture the spectral weight does not transfer.

However, it is still unclear whether the narrow peak appears or not on carrier doping; Romberg *et al.* concluded that no narrow impurity states were observed in their electron energy-loss spectroscopic experiments on $La_{2-x}Sr_xCuO_4$ (LSCO) [49]. On the contrary, in valence-band photoemission spectroscopic experiments on LSCO, Fujimori suggested the formation of the localized states and the narrow impurity band within the charge-transfer gap [41].

On the other hand, many theoretical studies have been also carried out to investigate the change of the electronic states on carrier doping. In the several studies using the $d-p$ model, which is one of the models which describes the CuO_2 plane [50, 51], the itinerant electronic state which appears on carrier doping was investigated.

The studies by using infinite-U_d models showed that the new electronic state is formed in the charge-transfer gap [52, 53, 54], and that the quasiparticle-like excitation peak appears and the charge-transfer gap is filled up [55] as the carrier concentration increases.

By the exact diagonalization of the two-dimensional cluster of 2×2 unit-cell system [56] and the one-dimensional cluster of Cu_4O_{13} [57], it was concluded that there is the peak structure corresponding to the singlet state caused by the $d-p$ hybridization in the insulating phase, and the Fermi level shifts into the peak and the system becomes metallic.

In the above theoretical studies, it was shown that in the metallic phase the peak structure exists near the Fermi level. However, there are differences between these results for the changes of the spectral function near the Mott transition; in the studies using the infinite-U_d model the peak structure near the Fermi level is absent in the insulating phase and grows with doping, and in the studies using the finite-size cluster the Fermi level shifts into the peak which already exists in the insulating phase.

Thus, there are some open questions. (1) Does a sharp peak structure emerge near the Fermi level when the carrier concentration increases ? (2) Does a singlet-state peak in the charge-transfer gap already exist at $n_{\rm tot}=1$?

In the present study, we would like to answer the above questions and to clarify the character of the itinerant electronic state in the metallic phase.

4.2 Numerical results

In the present section, we mainly show the numerical results of the one-particle-excitation spectral functions obtained by the quantum Monte Carlo (QMC) and the maximum entropy (ME) methods [1] .

We first survey the overall structure of the electronic states by plotting the number density of the electrons against the chemical potential, in Section 4.2.1. In Section 4.2.2, we show the spectrum at $n_{\rm tot} = 1$, where it is expected that the system is in the charge-transfer-type insulating phase. The spectra in the hole-doped and electron-doped cases are shown in 4.2.3 and 4.2.4, respectively. The results of doping dependence of mass enhancement are shown in 4.2.5. Throughout the present section, we mainly treat the case with $U_d = 5$ and $\Delta = 3$. (The energy is scaled by t.)

4.2.1 $\mu - n$ plots

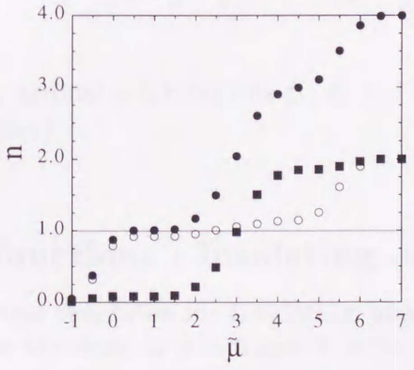

Figure 4.1: Plot of the total hole number density $n_{\rm tot}$ (solid circles), the d-hole number density n_d (open circles), and the p-hole number density n_p (solid squares) against the chemical potential. ($\tilde{\mu}$ is defined in the text.)

We show the number density n of holes as a function of the chemical potential μ [38]. Hereafter, we refer to such a plot as a $\mu - n$ plot. We mainly show

[1] We refer to the spectral function obtained by the QMC and ME methods as the QMC-ME spectral function.

$\mu - n$ plots at $\beta = 8$ and $L = 32$.

In Fig. 4.1, we show a typical $\mu - n$ plot. (The statistical error of the $\mu - n$ plot is discussed in Appendix B.1.) Note that the chemical potential is measured from d-level ε_d in the figure; we define $\tilde{\mu} \equiv \mu - \varepsilon_d$.

A remarkable fact is that a plateau develops at $n_{\rm tot} = 1$ for $0.5 \lesssim \tilde{\mu} \lesssim 1.5$. This implies that there is a gap and the system is an insulator at $n_{\rm tot} = 1$. The gap $E_{\rm gap}$ is estimated as $E_{\rm gap} \simeq 1$. As is expected, it is a charge-transfer-type insulator at $n_{\rm tot} = 1$, because (1) when the total number density increases from $n_{\rm tot} = 1$ ($\tilde{\mu} \gtrsim 2$), the d-hole number density remains almost constant $n_d \simeq 1$ before the p band is filled, and (2) the gap $E_{\rm gap}$ increases as a charge-transfer energy Δ increases (Fig. 4.2).

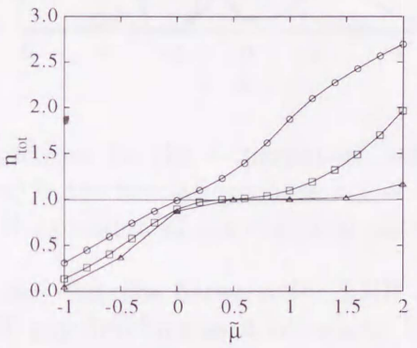

Figure 4.2: Plots of $n_{\rm tot}$ against μ for various Δ; $\Delta = 2$ (open circles), 3 (open squares), 4 (open triangles).

4.2.2 Spectral functions : insulating phase

We first show the spectral functions for insulating phase. Hereafter, we put $\varepsilon_p = 0$. We mainly show the data at $\beta = 8$ and $L = 64$.

In Fig. 4.3, we show the spectral functions for $n_{\rm tot} = 1.00$. We find that two large peaks develop around $\omega \sim \varepsilon_d$ and around $\omega \sim \varepsilon_d + U_d$ in $\rho^d(\omega)$; they should correspond to the lower Hubbard band (LHB) and the upper Hubbard band (UHB), respectively. On the other hand, the p-hole spectral weight is almost concentrated around $\omega = \varepsilon_p (= 0)$. [2] Both d- and p-hole spectral functions have a gap; it is the charge-transfer (CT) gap. The CT gap develops

[2] In the calculation of the p-component of spectral function $\rho^p(\omega)$ by the ME method, we should use the statistical errors for $G^p(\tau_l)$ themselves. However, we use the statistical errors for $G^d(\tau_l)$ for those for $G^p(\tau_l)$ for simplicity.

between the LHB and the p-band. The chemical potential is in the CT gap, and the system is in the insulating phase. [3]

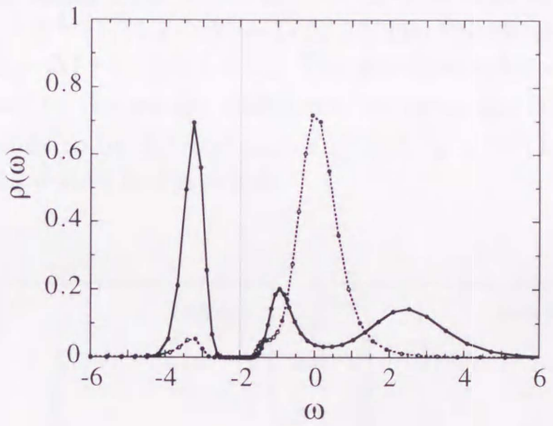

Figure 4.3: Spectral functions for the d-component (solid circles) and the p-component (open circles) in the insulating phase $n_{\rm tot} = 1.00$ at $\mu = -2.0$. The vertical thin line show the position of the chemical potential.

It is expected that the distance between the LHB and UHB increases as U_d increases and the CT gap develops as Δ increases. The QMC-ME spectral functions for the various sets of parameters, (U_d, Δ), are shown in Figs. 4.4. We find that the results are indeed consistent with the above expectations.

In Fig. 4.4, we also compare the spectral functions with those obtained by the single-cluster calculation. In each case, we can find that the positions of the spectral lines agree with the positions of the main peaks in the QMC-ME spectra. It suggests that the single-cluster calculation is valid in the insulating case.

The most remarkable fact in Fig. 4.4 is that the d-hole spectrum $\rho^d(\omega)$ has a peak just below $\omega = \varepsilon_p$. We investigate the hole-addition state corresponding to the peak by the single-cluster calculation. We analyze the case with $U = 5$ and $\Delta = 3$ in detail (Fig. 4.4(a)) (see Appendix D). The ground state $\Psi_{0\sigma}^{(1)}$ at $n_{\rm tot} = 1$ is dominantly a $|d^1\rangle$ state ($|a^d|^2 = 0.92$). The line corresponding to the peak ($\omega = -0.8$) we are interested in is caused by the transition to a singlet state $\Psi_0^{(2)}$ dominated by a $|d^1p^1\rangle$ state ($|a^{dp}|^2 = 0.76$). The spectral line appears below $\omega = \varepsilon_p$, because $\Psi_0^{(2)}$ reduces its energy eigenvalue by the d-p

[3] Strictly speaking, there is a finite intensity at the chemical potential. However, we refer to the present case $n_{\rm tot} = 1$ as an insulating phase, because the intensity at the chemical potential is smaller than 10^{-5}.

hybridization. This can be understood from the perturbation theory in the $d-p$ hybridization energy t applied to the single cluster. For $U_d \gg \Delta \gg t$, the energy of $\Psi_{0\sigma}^{(1)}$ shifts from ε_d to $\varepsilon_d - t^2/\Delta$ and that of $\Psi_0^{(2)}$ shifts from $\varepsilon_p + \varepsilon_d$ to $\varepsilon_p + \varepsilon_d - 2t^2/(1/(U_d - \Delta) + 1/\Delta)$. Thus, the spectrum line appears $\omega = \varepsilon_p - 2t^2(1/(U_d - \Delta) + 1/(2\Delta)) < \varepsilon_p$. The absolute value of the energy gain of $\Psi_0^{(2)}$ corresponds to the energy difference between the (d^1p^1) triplet state and $\Psi_0^{(2)}$, and it tends to be the exchange energy $2J_{\mathrm{K}} = 2t^2(1/(U_d - \Delta) + 1/\Delta)$ between a localized d-spin and a p-hole.

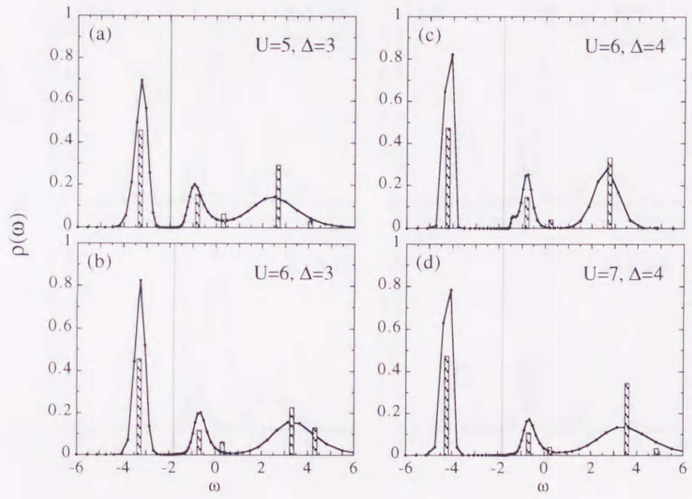

Figure 4.4: Comparison of QMC-ME spectral functions (solid line) with those obtained by the single-cluster calculation (hatched bars) for various sets of parameters, U_d and Δ ; (a) $(U_d, \Delta) = (5, 3)$, (b) $(6, 3)$, (c) $(6, 4)$, and (d) $(7, 4)$.

We can thus conclude that the central peak of $\rho^d(\omega)$ in the QMC-ME spectrum is dominantly caused by the hole-addition excitation from a d^1 state to a local d^1p^1 singlet state. Hereafter, we refer to the peak as the local $d-p$ singlet peak.

In Fig. 4.4, the LHB and UHB are observed at the positions slightly lower than ε_d and higher than $\varepsilon_d + U_d$, respectively. (The lower Hubbard level and the upper Hubbard level become ε_d and $\varepsilon_d + U_d$ in the atomic limit.) For $U_d \gg \Delta \gg t$, the energy of the state which is dominantly $|d^2\rangle$ shifts from $2\varepsilon_d + U_d$ to $2\varepsilon_d + U_d + 2t^2/(U_d - \Delta)$. Thus, the hole-removal excitation

energy corresponding to the LHB ($d^1 \rightarrow d^0$) becomes $\varepsilon_d - t^2/\Delta < \varepsilon_d$ and the hole-addition excitation energy corresponding to the UHB ($d^1 \rightarrow d^2$) becomes $\varepsilon_d + U_d + 2t^2/(U_d - \Delta) + t^2/\Delta > \varepsilon_d + U_d$.

4.2.3 Hole-doped case

In Figs. 4.5 we show the d-hole spectral functions $\rho^d(\omega)$ and the p-hole spectral functions $\rho^p(\omega)$ for different values of $n_{\rm tot}$: from $n_{\rm tot} = 1.00$ to 1.28.

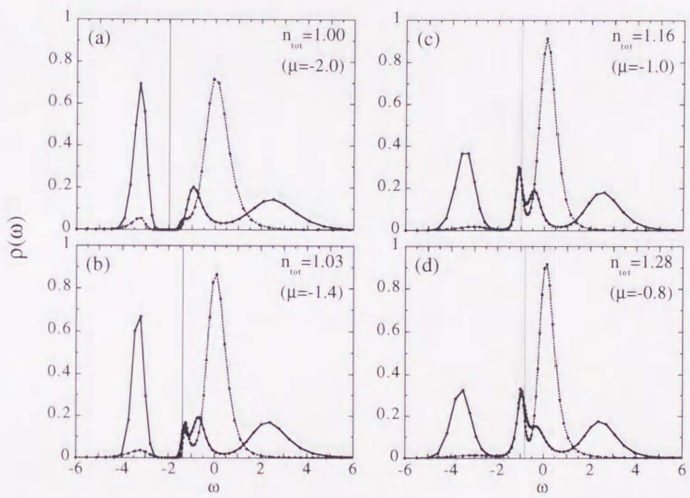

Figure 4.5: Carrier number dependence of the d- (solid circles) and the p- (open circles) components of the spectral functions: (a) $n_{\rm tot} = 1.00$ ($\mu = -2.0$), (b) 1.03 (-1.4), (c) 1.16 (-1.0), and (d) 1.28 (-0.8).

It is remarkable that when the system is doped with holes, a new peak develops below the local $d-p$ singlet peak, and the chemical potential shifts into the new peak. As the hole number increases, the new peak is sharply evolved, while the intensity of the LHB is decreasing (Figs. 4.5(b) and (c)). It shows that the spectral weight for the higher-energy-scale excitation transfers to the region near the chemical potential, and forms the sharp peak corresponding to itinerant states. In the metallic state, the p-hole spectral weight at the chemical potential is nearly the same as the d-hole spectral weight (Fig. 4.5(d)). This implies that p-holes and d-holes are strongly hybridized to form itinerant states.

In Fig. 4.6, we show the evolution of the new peak in the total spectral function $\rho_{\rm tot}(\omega) = \rho^d(\omega) + \rho^p(\omega)$. This shows that the new peak grows rapidly and the CT gap is filled up as the number density of holes increases.

We have found that upon doping a peak emerges near the local $d-p$ singlet peak and the corresponding electronic state becomes itinerant, and the itinerant state is formed by the strong hybridization between p-holes and d-holes. These suggest that the itinerant state in the metallic phase originates from a $d-p$ singlet state.

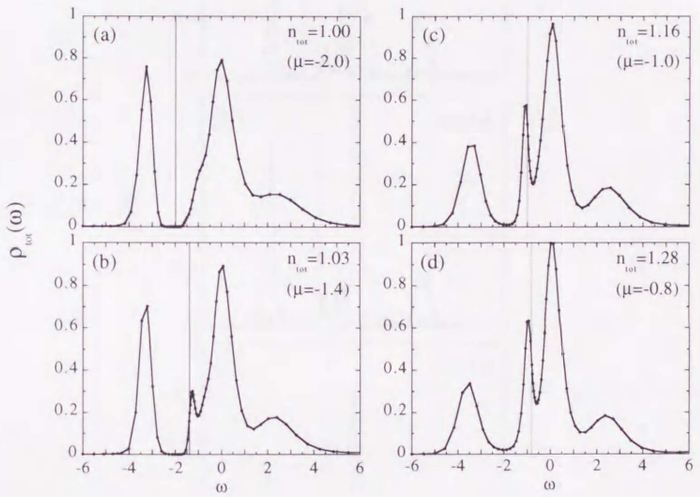

Figure 4.6: Carrier number dependence of the total spectral function $\rho_{\rm tot}(\omega)$: (a) $n_{\rm tot} = 1.00$ ($\mu = -2.0$), (b) 1.03 (-1.4), (c) 1.16 (-1.0), and (d) 1.28 (-0.8).

The suggestion is also supported by the exact diagonalization (ED) method within the DMFT framework (see Appendix C) [58]. In the method, we can obtain the information of the electronic state in the present model by investigating the corresponding electronic state in the impurity Anderson model which approximate the effective impurity problem in the DMFT. Figures 4.7 show the spectral functions obtained using the ED method (the ED spectra) [58]. We show the ED spectra at the same chemical potentials as those used in the calculation of the QMC-ME spectra (see Fig. 4.5). Though the spectral function can be calculated at any temperature for $N_s = 5$, [4] only the results

[4]Since one has to use the Lanczos method for the large-size cluster, the calculation for

at $\beta = 8$ are shown here. We have found few changes of the spectrum even at lower temperatures [58]. In the figures, δ-function peaks are replaced by Lorentzian peaks with the width = 0.1.

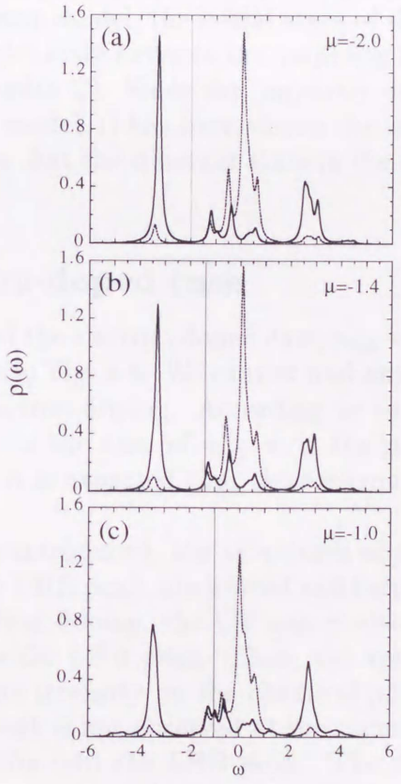

Figure 4.7: The ED spectra at various chemical potentials: (a) $\mu = -2.0$, (b) -1.4, (c) -1.0. Solid and broken lines indicate the d- and p-component of the spectrum, respectively.

We find that the all main peaks in the QMC-ME spectrum, such as the UHB, the LHB, the local $d-p$ singlet peak, and the large peak around $\omega \simeq \varepsilon_p (= 0)$ in ρ^p, also appear in the ED spectrum. [5] In the insulating phase

N_s larger than 5 can be carried out at only absolute zero.

[5] Though one cannot distinguish the metallic phase and the insulating phase by only the

(Fig. 4.7(a)), there is a peak caused by the transition from a d^1 state to a d^1p^1 singlet state just above the gap. (The peak corresponds to the local $d-p$ singlet peak in the QMC-ME spectrum.)

When the carriers are introduced into the system, the chemical potential shifts simply into the peak (Fig. 4.7(b), 4.7(c)). In the case of Fig. 4.7(c), in the impurity Anderson model, the initial state of the one-particle excitation is dominantly the singlet state between the 'impurity orbital' and the 'conduction electron' (see Appendix C). Since the 'impurity orbital' corresponds to the d hole in the original model, it has been shown the initial state is a $d-p$ singlet state [58]. It implies that the itinerant state in the metallic phase has the $d-p$ singlet character.

4.2.4 Electron-doped case

We have also studied the electron doped case, $n_{\rm tot} < 1$. The QMC-ME spectral functions are shown in Fig. 4.8. We cannot find any remarkable changes in the p-component on electron doping. According to the $\mu - n$ plot of the system (see Section 4.2.1), in the case of $n_{\rm tot} < 1$, the p-hole number density n_p is almost zero. Thus, it is expected that the electron doping does not affect the p-band.

As electrons are introduced, the structures of the hole-addition spectrum ($\omega > \mu$), such as the UHB peak, are leveled and turned into a broad single-peak structure. On electron doping, the CT gap is also filled in and the chemical potential shifts into the LHB peak. Then, the system becomes metallic (the spectrum has a finite intensity on the chemical potential). In this case, however, a prominent peak is not observed at the chemical potential; the chemical potential *simply* shifts into the LHB peak. The change in the chemical potential is thus asymmetric with respect to hole and electron doping in the charge-transfer-type insulators.

One of the possible reasons why the peak structure is not observed in the electron-doped case is the peculiar band structure of the present model (Section 3.3.1). In the free ($U_d = 0$) case, no peak structure forms at the chemical potential. Even in the interacting case, since the d-hole correlation effect decreases for the electron-doped case in the present model, it is possible that the peak structure does not appear in the electron-doped case. Another possibility is that the temperature in the present results is so high that the peak cannot be observed. A further study is needed to investigate these points in detail (see also Section 5.2.2).

---

spectral functions, we refer to the case at $\mu = 2.0$ as the insulating phase, for convenience.

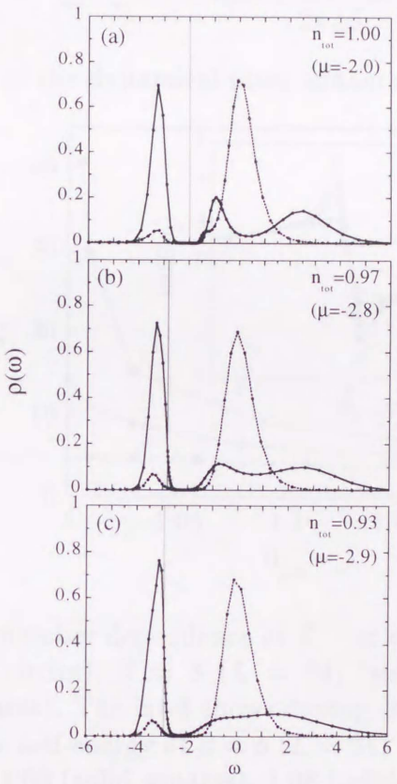

Figure 4.8: Carrier number dependence of the d- (solid circles) and the p- (open circles) components of the QMC-ME spectral functions in the electron-doped case ($n_{\rm tot} \leq 1$): (a) $n_{\rm tot} = 1.00(\mu = -2.0)$, (b) $0.97(-2.8)$, (c) $0.93(-2.9)$.

4.2.5 Mass enhancement factor

Finally, we estimate the mass enhancement from the imaginary part $\mathrm{Im}\Sigma(\mathrm{i}\omega_n)$ of the self-energy. We define the mass enhancement factor (or inverse of the renormalization factor) Z^{-1} as follows;

$$Z^{-1} \equiv 1 - \left. \frac{\partial \Sigma(\mathrm{i}\omega_n)}{\partial \mathrm{i}\omega_n} \right|_{\omega_n \to 0} \tag{4.1}$$

$$\simeq 1 - \frac{\mathrm{Im}\Sigma(\mathrm{i}\pi/\beta) - \mathrm{Im}\Sigma(-\mathrm{i}\pi/\beta)}{2\pi/\beta},$$

which is a measure of the dynamical mass enhancement.

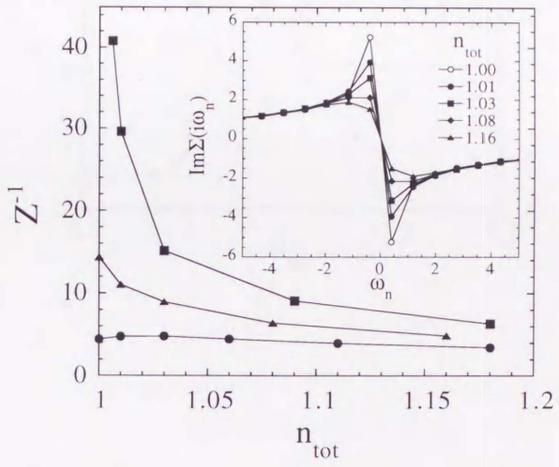

Figure 4.9: Carrier number dependence of Z^{-1} at different temperatures: $\beta = 4$ ($L = 32$) (solid circles), $\beta = 8$ ($L = 64$) (solid triangles) and $\beta = 16$ ($L = 64$) (solid squares). The inset shows doping dependence of the imaginary part $\mathrm{Im}\Sigma(\mathrm{i}\omega_n)$ of the self-energy at $\beta = 8$ ($L = 64$) : $n_{\mathrm{tot}} = 1.00$ (open circles), 1.01 (solid circles), 1.03 (solid squares), 1.08 (solid diamonds) and 1.16 (solid triangles).

In Fig. 4.9, we show the mass enhancement factor against $n_{\mathrm{tot}}(> 1)$ at different temperatures. We find that as the system approaches to an insulating phase, the effective mass of a d-hole is strongly enhanced. Besides, at lower temperature, Z^{-1} is rapidly enhanced. This implies that the heavy quasiparticles are formed near the insulating phase at lower temperatures.

We also compare the mass enhancement factor in the hole-doped case with that in the electron-doped case in Fig. 4.10. The mass enhancement factor is increasing as n_{tot} tends to 1 in both cases. While the enhancement factor is suppressed rapidly as the electrons are doped ($n_{\mathrm{tot}} < 1$), however, it is still large away from $n_{\mathrm{tot}} = 1$ in the hole-doped case ($n_{\mathrm{tot}} > 1$). The correlation in the hole-doped case is thus more effective than that in the electron-doped case.

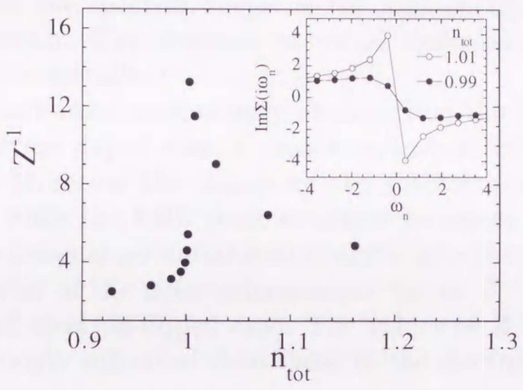

Figure 4.10: Carrier number dependence of Z^{-1} in the hole-doped case ($n_{\rm tot} > 1$) and the electron-doped case ($n_{\rm tot} < 1$) at $\beta = 8$ ($L = 64$). The inset shows the imaginary parts $\mathrm{Im}\Sigma(\mathrm{i}\omega_n)$ of the self-energy in the hole-doped case ($n_{\rm tot} = 1.01$: open circle) and the electron-doped case (0.99 : solid circle).

4.3 Summary and discussion

Summary

To summarize, we have calculated the spectral functions of the two-band charge-transfer-type system, and have obtained the continuous carrier number dependence of the spectral functions from the insulating phase to the metallic phase. We have studied the changes of the spectrum for the low-doping region which cannot be realized by the finite-size cluster.

What we have found are:

(1) When the total number density $n_{\rm tot} = 1$, a gap develops and the chemical potential is in it, and the system becomes a charge-transfer-type insulator for $U_d \gg \Delta \gg t$.

(2) In the insulating phase, there already exists the local $d-p$ singlet peak in the charge-transfer gap. In the total spectral function $\rho_{\rm tot}(\omega)$, the peak is not so prominent.

(3) As holes are doped, another new peak develops just below the local $d-p$ singlet peak, while the spectral weight in the high-energy region transfers to the low-energy region. The chemical potential shifts into the new peak and the system becomes metallic.

(4) The itinerant state continuously evolves from the $d-p$ singlet state.

(5) In the electron-doped case, a peak structure at the chemical potential is not observed. Moreover the change of the spectrum is different from the hole-doped case; while the UHB peak structure broadens, the LHB peak still remains and the chemical potential simply shifts into the LHB.

(6) The behavior of the mass enhancement factor Z^{-1} is also asymmetric with the hole- and electron-doped case. The values of Z^{-1} in the hole-doped case are more strongly enhanced than those in the electron-doped case.

Discussion

The mass enhancement factor should be compared with the coefficient γ of the temperature-linear term in the electronic specific heat. The experimental results of the high-T_c cuprates show the asymmetry of the values of γ; γ of the electron-doped cuprates [59, 60] is smaller than that of the hole-doped cuprates. [61] It is qualitatively consistent with our results. In the experiments, however, γ is not increasing when the system approaches to the Mott transition [59, 60, 61] in contradiction to the present results. This may suggest the effect of the momentum dependence of the self-energy becomes more important near the Mott transition.

The d^1p^1 singlet state in the present results corresponds to the $d^9\underline{L}$ singlet states in the electron representation. The existence of the $d^9\underline{L}$ local singlet states in the high-T_c cuprates was inferred from a photoemission experiment.[62] The authors emphasized that the singlet states *preexist* in the insulating phase. Numerical calculations for the cuprates [39, 40, 56, 57] also showed the formation of the local-singlet states in the insulating phase. Our calculations are consistent with those results.

Some other theoretical studies by using the $d-p$ model with the limit $U_d \to \infty$ show that there is no structure in the charge-transfer gap (i.e., between the LHB and the p-band) in the insulating phase and the new state arises around the Fermi level inside the charge-transfer gap only when the carriers are doped into the system [52, 53]. The behavior that the peak structure emerges near the Fermi level is consistent with our results.

We conclude that our result suggests a picture which connects the existence of the local $d-p$ singlet peak in the insulating phase and the emergence of the new peak structure corresponding to the itinerant state in the metallic phase.

Zhang and Rice [63] claimed that the electronic states of the high-T_c cuprates could be described in terms of the local-singlet states moving around the system. We have found the local $d-p$ singlet peak appearing below $\omega = \varepsilon_p$. It is caused by the energy gain of the strong hybridization between a d-hole and a p-hole. We have also clearly shown that the itinerant states in the metallic state originate from the local $d-p$ singlet states in the insulating phase. These results imply that the itinerant states locally have the character of the singlet states, and suggests the following scenario of the formation of the itinerant state; once holes are introduced, the local singlet states overlap with one another and form itinerant states, and the system turned into a metallic phase. The results supports the description of the metallic phase in terms of the local-singlet states for the low energy behavior.

Chapter 5

Mott-Hubbard-type systems

In the Mott-Hubbard-type systems, the energy level of the $2p$ orbital in the ligand anion lies away from the Fermi level and the charge-transfer energy Δ is larger than the Coulomb energy U_d between $3d$ electrons. The compounds of light transition-metal, Ti, V, and Cr belong to this type of materials.

In this chapter, we study the behavior of spectral functions and clarify how the spectral weight changes near the Mott transition when the ratio of the Coulomb energy to the $3d$ band width changes in the Mott-Hubbard-type system.

We briefly review some experimental results and theoretical analyses of the Mott-Hubbard-type transition-metal oxides, and show the purpose of the present study in Section 5.1. The numerical results of the Coulomb-energy dependence of the spectral functions are shown in Section 5.2. In the section, we also show the results of the mass-enhancement factors. In Section 5.3, we summarize and discuss the present results.

5.1 Introduction

Fujimori *et al.* studied the evolution of the spectral function in $SrVO_3$, $LaTiO_3$, and $YTiO_3$ by the photoemission spectroscopic experiment [64]. The strength of the effective electron correlation (the ratio of the Coulomb interaction energy to the $3d$ band width) increases in the order $SrVO_3 \rightarrow LaTiO_3 \rightarrow YTiO_3$. It was reported that the spectral weight is transferred from the region near the Fermi level to the high-energy region with increasing the effective electron correlation.

Inoue *et al.* then carried out a systematic study of $Ca_{1-x}Sr_xVO_3$ [65]. Both $CaVO_3$ and $SrVO_3$ are metallic. The correlation effect in $CaVO_3$ [66, 67] is

larger than that in $SrVO_3$ [68]. In $Ca_{1-x}Sr_xVO_3$, one can control the ratio of the Coulomb interaction energy to the $3d$ band width by substitution of Ca by Sr [65]. (The ratio of the Coulomb interaction energy to the band width increases when x decreases.) Inoue *et al.* reported that as the interaction becomes strong, (1) the weight is gradually transferred to the high energy region, and (2) the spectral intensity near the Fermi level simply decreases. The latter fact is in partial contradiction to the theoretical result for the single-band Hubbard model; in the model while the integrated intensity near the Fermi level decreases, the value of the spectral intensity at the Fermi level should be invariant. The authors ascribed the discrepancy to the $\boldsymbol{k}$-dependence of the self-energy, which is neglected in the infinite-dimensional model.

In the present study, we study the effect of the p orbital in the change of the spectral intensity at the Fermi level by using the two-band Hubbard model. In the two-band Hubbard model, even if the self-energy is $\boldsymbol{k}$-independent, the intensity at the Fermi level is not always invariant (see Appendix E). We also investigate how the spectral function changes in the present two-band model when the carriers are doped into the Mott-Hubbard-type system. In the study of the single-band Hubbard model by the DMFT [25], it was reported that a narrow resonance peak appears near the Fermi level when the filling decreases. We compare the results of the present study with those obtained using the single-band model, and discuss the consistency and the difference between the single-band and two-band model.

5.2 Numerical results

We first show, in Section 5.2.1, the $\mu - n$ plots (see also Sec. 4.2.1) for various parameters to survey the overall structure the electronic states of the present system. After showing a typical spectrum of the Mott-Hubbard-type insulator, we show the evolution of the spectral functions when the Coulomb interaction energy U_d becomes strong in Section 5.2.2. We also compare the spectra with those obtained using the single-cluster calculation. Finally, the doping dependence of the spectral functions are shown in 5.2.3. [1]

Throughout the present section, we fix the charge-transfer energy as $\Delta = 4$.

[1] In the present section, we refer to the fermions which we consider as "holes" to avoid the confusion, although in the real Mott-Hubbard-type perovskite transition-metal oxides the stable electron configuration of the transition-metal ion (Ti^{3+} or V^{4+}) is $3d^1$.

5.2.1 $\mu - n$ plots

In Fig. 5.1, we show a typical $\mu - n$ plot of the Mott-Hubbard-type system at $\beta = 8$ and $L = 32$. In the plot, a plateau is observed at $n_{\rm tot} = 1$ in addition to

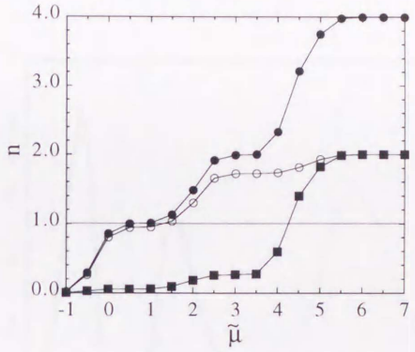

Figure 5.1: Plot of the total hole number density $n_{\rm tot}$ (solid circles), d-hole number density n_d (open circles), and p-hole number density n_p (solid squares) against the chemical potential for $U_d = 2.5$.

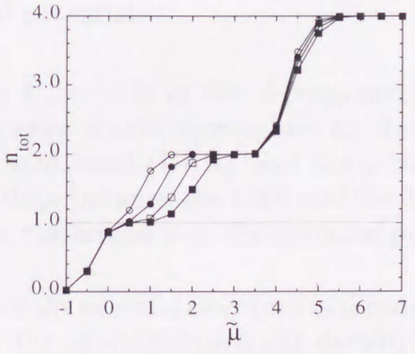

Figure 5.2: Plot of the total hole number density $n_{\rm tot}$ against the chemical potential for various U_d; $U_d = 1.0$ (open circles), 1.5 (solid circles), 2.0 (open squares), and 2.5 (solid squares).

a plateau at $n_{\rm tot} = 2$, which corresponds to a conventional band gap. We find that n_d is increasing faster than n_p in the region $n_{\rm tot} \geq 1$. Thus, the plateau means that the Mott-Hubbard gap develops at $n_{\rm tot} = 1$. We also find that as the strength of U_d increases, the Mott-Hubbard gap increases (Fig. 5.2).

5.2.2 Spectral functions : U_d dependence

We first show a typical spectrum in the Mott-Hubbard-type insulating phase. Figure 5.3 provides the spectral functions of d- and p-components for $U_d = 2$ (hereafter we show the data for $L = 64$). We find that there are large peaks

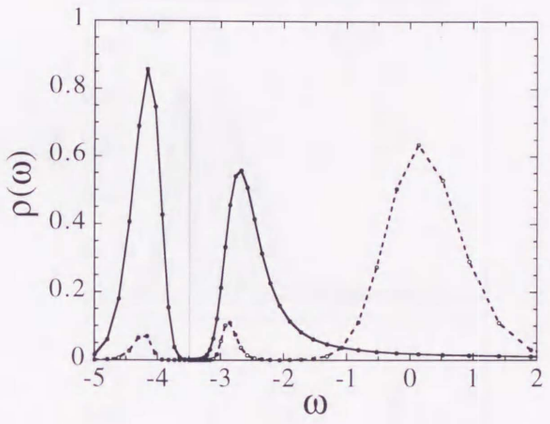

Figure 5.3: Spectral function of d- (solid circles) and p-components (open circles) for $U_d = 2$ at $\mu = -3.5$ and $\beta = 8$. The vertical thin lines show the position of the chemical potential.

around $\varepsilon_d(= -4)$, $\varepsilon_d + U_d(= -2)$ in the d-component, and $\varepsilon_p(= 0)$ in the p-component. These peaks should correspond to the lower Hubbard band (LHB), the upper Hubbard band (UHB), and the p band, respectively. The Mott-Hubbard gap develops between the LHB and the UHB, and the chemical potential sits in the gap; the intensity at the chemical potential is smaller than 10^{-5}.

The U_d dependence of the spectral functions is shown in Fig. 5.4(a) and (b). It is clearly shown that the Mott-Hubbard gap develops as U_d increases. The intensity of the UHB of the d-component decreases and the spectral weight transfers to higher-frequency region. It is also observed that the intensity of the p-band decreases and the spectral weight transfers into the band gap between the UHB and the p-band in the p-component spectrum. The behavior is understood qualitatively as follows. In the present case of $\Delta = 4$, as the strength of U_d is increasing and is close to Δ, the difference of energy of the hole addition excitation to the UHB and to the p-band is decreasing. Thus, the intensity of the UHB is suppressed as U_d increases, while that of the p-band is enhanced. The band gap between the UHB and the p-band is filled up.

We cannot find a sharp peak structure at the chemical potential for any value of U_d. This is a marked difference from the results obtained for the single-band Hubbard model by Jarrell et al. [25]. This point will be discussed in Section 5.3.

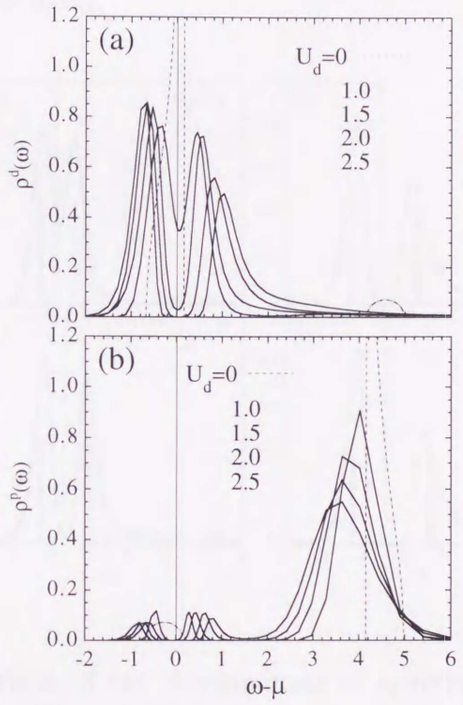

Figure 5.4: (a) d-components and (b) p-components of spectral functions (solid lines) for the various U_d; $U_d = 1.0, 1.5, 2.0$, and 2.5 (from top to bottom). For comparison, we also show the spectra for $U_d = 0$ obtained analytically (broken thin lines). Note that we set the origin of frequency to the chemical potential.

Figure 5.5 provides the comparison of the d-component of the spectral functions obtained using the QMC and ME method with those obtained using the single-cluster calculation. For each value of U_d, both of the two peaks (referred to as the LHB and UHB so far) in the spectrum obtained by the QMC and ME methods are consistent with the two large peaks obtained by the single-cluster calculation. The lower peak corresponds to the hole-removal

excitation dominated by $d^1 \rightarrow d^0$ and the upper one corresponds to the hole-addition excitation dominated by $d^1 \rightarrow d^2$. (For example, $|a^d|^2 = 94.7\%$ in the one-particle ground state and $|a|^2 = 84.3\%$ in the two-particle ground state for $U_d = 1.0$. The meaning of the coefficients a^d and a^{dd} is shown in Appendix D.) Therefore it is reasonable to call the two large peaks the lower and upper Hubbard band, respectively.

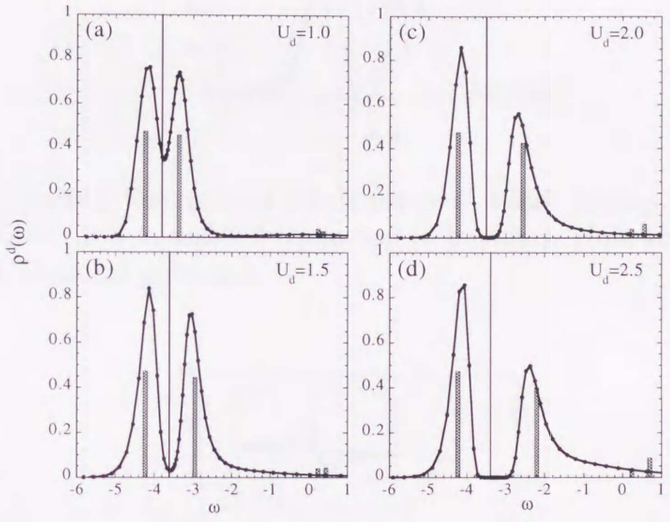

Figure 5.5: Comparison of the d-component of spectral functions obtained using the QMC and ME methods (solid line) with those obtained using the single-cluster calculation (hatched bars) for the various U_d; (a) $U_d = 1.0$, (b) 1.5, (c) 2.0, and (d) 2.5. The vertical thin lines show the position of the chemical potential.

We also find that the percentage of the $|d^2\rangle$ state in the final state of the UHB decreases as U_d increases. For $U_d = 1.0$, the percentage of the $|d^2\rangle$ state is 84.3% and that of the $|d^1p^1\rangle$ singlet state is 15.2%. On the other hand, for $U_d = 2.5$, the former is 68.4% and the latter is 30.2%. This result supports the qualitative explanation for the decrease of the intensity of the UHB in the QMC-ME spectrum for large U_d.

Since the single-cluster calculation is valid only in the insulating phase, as mentioned in Section 4.2.2, it is not suitable to investigate the itinerant state near the chemical potential in the metallic phase for $U_d \lesssim 1.5$. Namely, we cannot answer the question whether a sharp peak structure is formed at the

chemical potential or not by using only the single-cluster calculation.

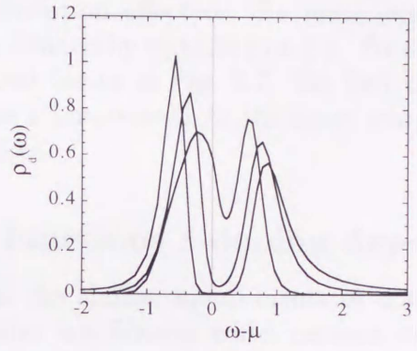

Figure 5.6: Spectral functions of d-hole for $\Delta = 4$ and various U_d at $\beta = 16$ ($L = 64$); $U_d = 1.0$, 1.5, and 2.0 (from top to bottom). Note that we set the origin to the chemical potential.

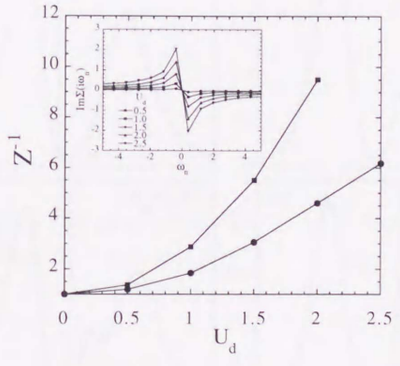

Figure 5.7: Plot of the mass enhancement factor Z^{-1} against U_d at $\beta = 8$ (solid circles) and $\beta = 16$ (solid squares). The inset shows the imaginary parts of the self-energy at $\beta = 8$ for the various U_d; $U_d = 0.5$ (solid circles), 1.0 (open circles), 1.5 (solid squares), 2.0 (open squares), and 2.5 (solid triangles).

A peak structure can be observed if the temperature is further decreasing. In Fig. 5.6, we show the spectral functions for various U_d at $\beta = 16$. Even at the lower temperatures, however, a sharp peak structure at the chemical potential is not observed. This point is later discussed in detail.

Mass enhancement factor

We investigate the correlation effect on the mass enhancement factor Z^{-1}, which has been already defined by eq.(4.2) in 4.2.5. We show the U_d-dependence of the mass enhancement factor in Fig. 5.7. We find that the mass enhancement factor increases as U_d increases. At the lower temperatures, the effective mass is strongly enhanced.

5.2.3 Spectral functions : doping dependence

It is also expected that the similar metal-insulator transition occurs and the itinerant electronic states are formed when carriers are introduced into the system. We study the evolution of the d-component of the spectral function on carrier doping as we did for the charge-transfer-type system.

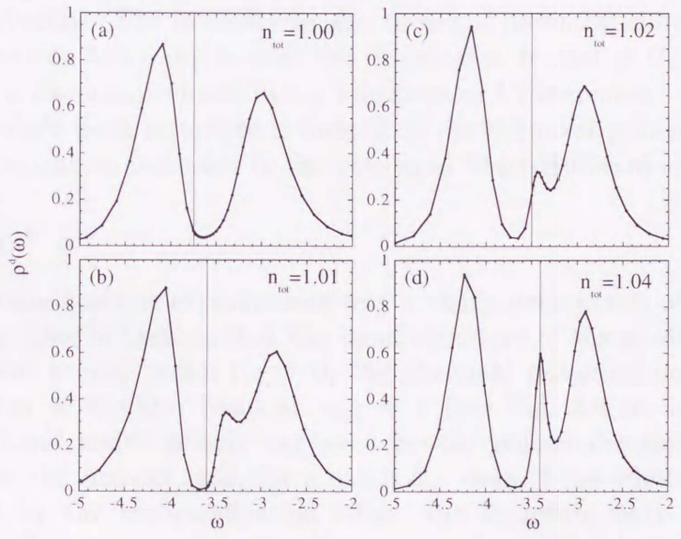

Figure 5.8: Spectral functions of d-hole for various total hole density $n_{\rm tot}$ at $\beta = 16$; (a) $n_{\rm tot} = 1.00$, (b) 1.01, (c) 1.02, and (d) 1.04. The vertical thin lines show the position of the chemical potential.

Figures 5.8 provide the d-components of the spectral functions for various values of the total hole density $n_{\rm tot}$. We find that a peak structure is formed and growing at the position just below the UHB when the total hole density $n_{\rm tot}$ increases . The chemical potential shifts into the growing peak. This

implies that the change of the spectrum is not rigid-band-like and the peak structure which corresponds to the itinerant electronic state emerges when the carrier concentration increases.

5.3 Summary and discussion

Summary

To summarize, we have studied the spectral functions and the mass enhancement factor near the Mott transition in the two-band Mott-Hubbard system.

What we have found are the following.

(1) As U_d increases the Mott-Hubbard gap develops at the chemical potential in the spectral function.

(2) For any value of U_d, a sharp peak structure has not been observed at the chemical potential. The intensity at the chemical potential simply decreases, and the spectrum has a dip around the chemical potential as U_d increases.

(3) The mass enhancement factor increases as U_d increases.

(4) A narrow peak structure is formed at the chemical potential when the carrier concentration increases in the two-band Mott-Hubbard system.

Discussion

There are some possible explanations why a sharp peak is not observed when U_d increases. One of them is that the band structure of the model is peculiar. In the present model, when $U_d = 0$, the chemical potential does not sit in the maximum of the free band at $n_{\mathrm{tot}} = 1$ (see Fig. 3.4 in Section 3.3.1). The whole band width is only narrowed by the renormalization effect for a small U_d. In the present case, for a small U_d, even if the whole band width is narrowed by the renormalization effect, the structure near the chemical potential is almost invariant, i.e., it does not form a peak structure. (On the contrary, for the single-band Hubbard model in the half-filled case, the spectrum at the chemical potential becomes a sharp peak which corresponds to the narrowed whole band, because the chemical potential always sits in the maximum of the band.)

On the other hand, for a large U_d, the peak structure cannot be observed when the temperature is so high. Jarrell reported that the peak structure at the chemical potential is very sensitive to the temperature [25]. In the study of the two-band Hubbard model using the modified IPT (see Section 2.2) [69], it was also pointed out that the peak structure near the chemical potential

rapidly diminishes, and no trace of the peak is found when the temperature is comparable to the width of it.

We estimate the width of a possible peak at lower temperatures at the chemical potential. The quasiparticle band width Γ^* is renormalized by the electron correlation as $\Gamma^* = Z\Gamma$, where Γ is the band width in the free system. If we take the d-band width of the free two-band model as Γ (see Fig. 3.4), Γ is estimated as $\Gamma \simeq 0.83$ for $\Delta = 4$. Note that we take $t = 1$ as the energy unit (see Section 3.3.1). Thus, the quasiparticle band width Γ^* is estimated as $\Gamma^* = Z\Gamma \sim 0.15$ (for $U_d = 2.5$) at $T = 0.125$ ($\beta = 8$). Namely, the temperature $T = 0.125$ is comparable to a possible band width of the quasiparticle. At the lower temperature $T = 0.0625$, the effective mass is strongly enhanced. For $U_d = 2.0$, a possible band width is estimated as $\Gamma^* \sim 0.08$. It shows that even at the lower temperatures ($T = 0.0625$) the possible band width is also comparable to the temperature. Thus, for a large U_d, the peak structure can be suppressed by the temperature in the present results.

It is a future problem to study the effect of band structure in detail. In order to obtain a definite conclusion about the formation of the peak structure in the spectral function, it is also needed to study the system at lower temperature.

We have found that the mass enhancement factor increases as U_d increases in the present results. In the experimental result, however, it was reported that the mass enhancement factors estimated from the specific heat coefficient, the Pauli-paramagnetic susceptibility [70], and the photoemission spectrum [65, 71] are not so enhanced when the correlations become strong in $Ca_{1-x}Sr_xVO_3$. In the experimental study by the photoemission spectroscopy (PES), the mass enhancement factor is estimated by fitting PES data with the spectrum in which one assumes the phenomenological self-energy. In the result, when the local self-energy is assumed, the effective mass is strongly enhanced. Thus, it was pointed out that it is difficult to explain the effective mass in the real system without considering the $\boldsymbol{k}$-dependence of the self-energy [65]. Besides, in Ref. [71], Inoue *et al.* suggested that it is important to consider the long-range interaction in order to explain the absence of the large mass enhancement. It is still an open problem whether the effective mass near the Mott transition is enhanced or not in the presence of the long-range interaction.

On the other hand, in connection with the analysis of the PES spectrum, it was also pointed out the importance of the randomness and surface effects in the sample materials. [72, 73]. Sarma *et al.* pointed out that with taking into account the inhomogeneity of real systems one can provides results which are in agreement with the experimental results even if one assumes that the self-energy is local. This shows that the inhomogeneity of real systems can be

important to analyze the spectrum obtained by the high-energy spectroscopic experiments quantitatively, although the effect of the long-range interaction may also be important.

In the carrier concentration dependence of the spectrum, the formation of the narrow peak at the chemical potential implies that the renormalized band of quasiparticle characterized by a certain energy scale (which corresponds to the width of the peak) is formed when the carrier concentration increases. The similar behavior was also observed in the spectral function obtained by the DMFT in the single-band Hubbard model [25]. This suggests that the description of the system in terms of the single-band model is valid as long as we consider the low-energy region.

Chapter 6

Concluding remarks

Throughout the thesis, we calculate the one-particle-excitation spectral function, and study the electronic states near the Mott transition in the two-band Hubbard model by the DMFT framework.

We have shown that the change of the spectral function on carrier doping is not rigid-band like one, and the peak structure corresponding to the itinerant electronic states emerges near the chemical potential in the metallic side of the Mott transition. These results suggest that the itinerant electronic state is characterized by the energy scale corresponding to the width of the sharp peak at the chemical potential.

It is also shown from the results that the quantum Monte Carlo method and the maximum entropy method within the DMFT framework are useful to describe the behavior of the spectral function near the Mott transition.

When we discuss the physics in the low-energy scale such as the dispersion of the quasiparticle near the chemical potential, or the physics in the case that the antiferromagnetic fluctuation becomes strong, the momentum dependence of the self-energy becomes important, and an improved approximation is necessary.

However, we can conclude that the description of the strongly correlated system using the DMFT is valid as long as we do not treat the properties in the low-energy region. We would like to emphasize that the DMFT is one of the useful methods to treat the correlation effects.

Future problems

There are some future problems.

- We need to consider a more realistic model, in which we treat the degeneracy of the d orbitals or the realistic band structure, in order to study

the Mott transition or other phenomena in the real transition-metal compounds.

- In order to discuss the property at lower temperatures, the quantum Monte Carlo method is not suitable. We are also interested in the method by which we can investigate the property of the system at low temperature including absolute zero within the DMFT framework (e.g. the modified IPT method [29]).

Appendix A

Derivation of the effective action

In this appendix, we show the derivation of the effective action in the infinite-dimensional limit [16]. We consider the single-band Hubbard model for simplicity.

The Hamiltonian of the single-band Hubbard model is defined as follows;

$$\mathcal{H} = -\sum_{<i,j>,\sigma} t_{ij}(c_{i\sigma}^{\dagger}c_{j\sigma} + \text{H.c.}) + U\sum_{i} c_{i\uparrow}^{\dagger}c_{i\uparrow}c_{i\downarrow}^{\dagger}c_{i\downarrow} - \mu\sum_{i\sigma} c_{i\sigma}^{\dagger}c_{i\sigma}. \tag{A.1}$$

The partition function Z of the system is expressed by

$$\begin{aligned} Z &= \text{Tr}e^{-\beta\mathcal{H}} \\ &= \lim_{N\to\infty} \text{Tr}(e^{-\beta\mathcal{H}/N})^N = \lim_{N\to\infty} \text{Tr}(1-\epsilon\mathcal{H})^N \\ &\equiv \lim_{N\to\infty} \text{Tr}Z_N, \end{aligned} \tag{A.2}$$

where $\epsilon \equiv \beta/N$. In the path-integral formulation, the partition function Z_N is expressed by the Grassmann variables $\{\ \bar{\psi}, \psi\ \}$ as follows;

$$Z_N = \int \prod_{n=1}^{N} \left\{ \prod_{i\sigma} \mathrm{d}\bar{\psi}_{i\sigma}^{(n)} \mathrm{d}\psi_{i\sigma}^{(n)} \exp\left[\epsilon \sum_{i\sigma} \left(\frac{\bar{\psi}_{i\sigma}^{(n+1)} - \bar{\psi}_{i\sigma}^{(n)}}{\epsilon} \psi_{i\sigma}^{(n)} - K(\{\bar{\psi}_{i\sigma}^{(n+1)}\}, \{\psi_{i\sigma}^{(n)}\}) \right) \right] \right\}, \tag{A.3}$$

where $K(\{\bar{\psi}_{i\sigma}^{(n+1)}\}, \{\psi_{i\sigma}^{(n)}\})$ is the "Hamiltonian" expressed by the Grassmann variables, and $\bar{\psi}_{i\sigma}^{(n)}$ and $\psi_{i\sigma}^{(n)}$ in K are arranged in the normal order. We obtain the path-integral expression of Z as follows;

$$Z = \int \prod_{i\sigma} \mathcal{D}\bar{\psi}_{i\sigma}\mathcal{D}\psi_{i\sigma} e^{-\mathcal{S}}, \tag{A.4}$$

where $\mathcal{S}$ is the action defined as;

$$\mathcal{S} \equiv \int_0^\beta \mathrm{d}\tau \tag{A.5}$$
$$\{\sum_{i\sigma} \bar{\psi}_{i\sigma}(\tau)\left(\frac{\partial}{\partial\tau} - \mu\right)\psi_{i\sigma}(\tau) - \sum_{\substack{i,j \\ \sigma}} t_{ij}\bar{\psi}_{i\sigma}(\tau)\psi_{j\sigma}(\tau) + U\sum_i \bar{\psi}_{i\uparrow}(\tau)\psi_{i\uparrow}(\tau)\bar{\psi}_{i\downarrow}(\tau)\psi_{i\downarrow}(\tau)\}.$$

Let us consider the effective action $\mathcal{S}_{\mathrm{eff}}$ defined by

$$\frac{1}{Z_{\mathrm{eff}}} e^{-\mathcal{S}_{\mathrm{eff}}[\bar{\psi}_{o\sigma},\psi_{o\sigma}]} \equiv \frac{1}{Z}\int \Pi_{\substack{i\neq o \\ \sigma}} \mathcal{D}\bar{\psi}_{i\sigma}\mathcal{D}\psi_{i\sigma} e^{-\mathcal{S}}. \tag{A.6}$$

First, we divide $\mathcal{S}$ into three parts;

$$\mathcal{S} = \mathcal{S}^{(0)} + \mathcal{S}_o + \Delta\mathcal{S}, \tag{A.7}$$
$$\mathcal{S}_o \equiv \int_0^\beta \mathrm{d}\tau\{\sum_\sigma \bar{\psi}_{o\sigma}(\tau)(\frac{\partial}{\partial\tau} - \mu)\psi_{o\sigma}(\tau) + U\bar{\psi}_{o\uparrow}(\tau)\psi_{o\uparrow}(\tau)\bar{\psi}_{o\downarrow}(\tau)\psi_{o\downarrow}(\tau)\},$$
$$\Delta\mathcal{S} \equiv -\int_0^\beta \mathrm{d}\tau\{\sum_{i\sigma} t_{io}\{\bar{\psi}_{i\sigma}(\tau)\psi_{o\sigma}(\tau) + \bar{\psi}_{o\sigma}(\tau)\psi_{i\sigma}(\tau)\}, \tag{A.8}$$
$$\equiv -\int_0^\beta \mathrm{d}\tau\{\sum_{i\sigma}\{\bar{\psi}_{i\sigma}(\tau)\eta_{i\sigma}(\tau) + \bar{\eta}_{i\sigma}(\tau)\psi_{i\sigma}(\tau)\},$$

where $\mathcal{S}^{(0)}$ denotes the action excluded a certain site o, and $\eta_{i\sigma} \equiv t_{io}\psi_{o\sigma}$ and $\bar{\eta}_{i\sigma} \equiv t_{io}\bar{\psi}_{o\sigma}$. We calculate the effective action as follows;

$$e^{-\mathcal{S}_o}\frac{1}{Z}\int \Pi_{\substack{i\neq o \\ \sigma}} \mathcal{D}\bar{\psi}_{i\sigma}\mathcal{D}\psi_{i\sigma} e^{-\mathcal{S}^{(0)}} e^{-\Delta\mathcal{S}} = e^{-\mathcal{S}_o}\frac{Z^{(0)}}{Z} < e^{-\Delta\mathcal{S}} >^{(0)}, \tag{A.9}$$
$$\equiv \frac{e^{-\mathcal{S}_{\mathrm{eff}}}}{Z_{\mathrm{eff}}},$$

where $< \cdots >$ is defined by

$$\frac{1}{Z}\int \Pi_{\substack{i\neq o \\ \sigma}} \mathcal{D}\bar{\psi}_{i\sigma}\mathcal{D}\psi_{i\sigma} \cdots e^{-\mathcal{S}^{(0)}}. \tag{A.10}$$

Carrying out the cumulant expansion,

$$< e^{-\Delta\mathcal{S}} >^{(0)} = \exp(\sum_{n=1}^{\infty} < \Delta\mathcal{S}^{2n} >_{\mathrm{c}}^{(0)}), \tag{A.11}$$

we can obtain the effective action as follows;

$$\mathcal{S}_{\text{eff}} = \sum_{n=1}^{\infty} \sum_{\substack{i_1 \cdots i_n \\ j_1 \cdots j_n}} \int \Pi_{\{i\}\{j\}} \mathrm{d}\tau_{i_1} \cdots \mathrm{d}\tau_{i_n} \mathrm{d}\tau_{j_1} \cdots \mathrm{d}\tau_{j_n} \bar{\eta_{i_1}}(\tau_{i_1}) \cdots \bar{\eta_{i_n}}(\tau_{i_n}) \eta_{j_1}(\tau_{j_1}) \cdots \eta_{j_n}(\tau_{j_n})$$

$$G^{(0)}_{\substack{i_1 \cdots i_n \\ j_1 \cdots j_n}}(\tau_{i_1}, \ldots, \tau_{i_n}; \tau_{j_1}, \ldots, \tau_{j_n}) + \mathcal{S}_o, \tag{A.12}$$

where

$$G^{(0)}_{\substack{i_1 \cdots i_n \\ j_1 \cdots j_n}}(\tau_{i_1}, \ldots, \tau_{i_n}; \tau_{j_1}, \ldots, \tau_{j_n}) \equiv < \bar{\psi}_{i_1}(\tau_{i_1}) \cdots \bar{\psi}_{i_n}(\tau_{i_n}) \psi_{j_1}(\tau_{j_1}) \cdots \psi_{j_n}(\tau_{j_n}) >^{(0)}_{\text{c}} . \tag{A.13}$$

Let us estimate each term in n-summation of (A.12) by simple power counting. Note that $\eta_i \sim 1/\sqrt{z}$ because of the scaling of $t_{ij} \sim (1/\sqrt{z})^{|i-j|}$.

1. (1): $n = 1$ $(G^{(0)}_{ij})$
   Since $i \neq j$ and $i, j \neq o$, the distance between i and j is $|i-j| = 2$ at least. The summations give a factor of order z; $\sum_i \sim z$ and $\sum_j \sim z - 1 \sim z$. Since $G^{(0)}_{ij} \sim (1/\sqrt{z})^{|i-j|}$, we obtain the overall factor of $n = 1$ term as

$$\sum_{ij} \bar{\eta}_i \eta_j G^{(0)}_{ij} \sim z^2 (\frac{1}{\sqrt{z}})^2 (\frac{1}{\sqrt{z}})^2, \tag{A.14}$$

$$\sim \mathcal{O}(1).$$

2. (2): $n = 2$ $(G^{(0)}_{ijkl})$

   (a) (2-1): the case in which i, j, k, l are all different.
   Since $G^{(0)}_{ijkl} \sim (1/\sqrt{z})^{|i-j|} (1/\sqrt{z})^{|i-k|} (1/\sqrt{z})^{|i-l|} \sim z^{-3}$ and a factor z^4 is given by four summations; $\sum_i \sim z$, $\sum_j \sim z - 1$, $\sum_k \sim z - 2$, and $\sum_l \sim z - 4$, we obtain the overall factor as

$$\sum_{ijkl} \bar{\eta}_i \bar{\eta}_j \eta_k \eta_l G^{(0)}_{ijkl} \sim z^{-1}. \tag{A.15}$$

   (b) (2-2): the case in which $i = j$ and $i \neq k, l$
   Since $G^{(0)}_{iikl} \sim (1/\sqrt{z})^{|i-k|} (1/\sqrt{z})^{|i-l|} \sim z^{-2}$ and a factor z^3 is given by three summations; $\sum_i \sim z$, $\sum_k \sim z - 1$, and $\sum_l \sim z - 2$, we obtain the overall factor as

$$\sum_{ikl} \bar{\eta}_i \bar{\eta}_i \eta_k \eta_l G^{(0)}_{iikl} \sim z^{-1}. \tag{A.16}$$

It is shown similarly that the overall factor of each term is at least of the order of $(1/z)^{n-1}$. Thus, only $n = 1$ term, i.e., the term of the two-point cumulant survives in the limit $z \to \infty$. Hence, we can obtain the final expression of the effective action in the infinite-dimensional limit;

$$\begin{aligned}
\mathcal{S}_{\text{eff}} &= \sum_{\substack{i,j \\ \sigma}} \int_0^\beta \int_0^\beta \mathrm{d}\tau \mathrm{d}\tau' \bar{\eta}_{i\sigma}(\tau) \eta_{j\sigma}(\tau') G^{(0)}_{ij\sigma}(\tau, \tau') \\
&+ \int_0^\beta \mathrm{d}\tau \{ \sum_\sigma \bar{\psi}_{o\sigma}(\tau) (\frac{\partial}{\partial \tau} - \mu) \psi_{o\sigma}(\tau) + U \bar{\psi}_{o\uparrow}(\tau) \psi_{o\uparrow}(\tau) \bar{\psi}_{o\downarrow}(\tau) \psi_{o\downarrow}(\tau) \}, \quad \text{(A.17)} \\
&\equiv - \int_0^\beta \int_0^\beta \mathrm{d}\tau \mathrm{d}\tau' \sum_\sigma \bar{\psi}_{o\sigma}(\tau) \mathcal{G}^{-1}(\tau - \tau') \psi_{o\sigma}(\tau) + U \bar{\psi}_{o\uparrow}(\tau) \psi_{o\uparrow}(\tau) \bar{\psi}_{o\downarrow}(\tau) \psi_{o\downarrow}(\tau),
\end{aligned}$$

where $\mathcal{G}$ is defined by

$$\mathcal{G}^{-1}(\tau - \tau') \equiv \delta(\tau - \tau')(\mu - \frac{\partial}{\partial \tau'}) - \sum_{i,j} t_{io} t_{jo} G^{(0)}_{ij\sigma}(\tau, \tau'). \quad \text{(A.18)}$$

Appendix B

The Hirsch-Fye algorithm and the maximum entropy method

In Section B.1, we show the Hirsch-Fye algorithm [28] of the quantum Monte Carlo method to solve the effective impurity problem in the DMFT as mentioned in Section 2.2. We can obtain the imaginary-time local Green's function of the system by the algorithm. In order to obtain the one-particle-excitation spectral functions from the imaginary-time local Green's function, we use the maximum entropy method [74, 75, 76]. The detailed explanation of the maximum entropy method is given in Section B.2.

B.1 Hirsch-Fye algorithm of the quantum Monte Carlo method

B.1.1 Hirsch-Fye algorithm

In the Hirsch-Fye algorithm [28], we start from a Hamiltonian which describe a system of an impurity interacting with conduction electrons.

$$\begin{aligned} H &= H_0 + H_1, \\ H_1 &\equiv U\left(n_\uparrow^d n_\downarrow^d - \tfrac{1}{2}\textstyle\sum_\sigma n_\sigma^d\right). \end{aligned} \tag{B.1}$$

In the DMFT, the impurity site, of which occupation number is described by n_σ^d, corresponds to a certain site o on the original sublattice M of the two-band Hubbard model, and the degree of freedom described by H_0 correspond to the effective medium (the dynamical mean field) excluding the site o.

By using the Suzuki-Trotter breakup, the partition function of the system is approximated for large $L \gg 1$ (L is the Trotter number) as follows;

$$Z \equiv \mathrm{Tr} e^{-\beta H} = \mathrm{Tr} \prod_{l=1}^{L} e^{-\Delta\tau H} \tag{B.2}$$

$$\simeq \mathrm{Tr} \prod_{l=1}^{L} e^{-\Delta\tau H_0} e^{-\Delta\tau H_1}, \tag{B.3}$$

where $\Delta\tau = \beta/L$. We decouple H_1 by the discrete Hubbard-Stratonovich transformation with Ising variable s as,

$$e^{-\Delta\tau H_1} = \exp\left\{-\Delta\tau U \left(n_\uparrow^d n_\downarrow^d - \frac{n_\uparrow^d + n_\downarrow^d}{2}\right)\right\} \tag{B.4}$$

$$= \frac{1}{2} \sum_{s=\pm} e^{\lambda s (n_\uparrow^d + n_\downarrow^d)}, \tag{B.5}$$

where λ is defined as $\cosh\lambda \equiv e^{\Delta\tau U/2}$.

The local Green's function $G^d(\tau_l)$ of the d-hole at the discrete time $\tau_l = (l-1)\Delta\tau$ ($l = 1, \ldots, L$) is obtained as the Monte Carlo expectation value of the element $g(l,l')$ of the Green's function matrix for a certain configuration of $\{s_l\}$. According to Hirsch and Fye, there is a relation between the Green's function matrix elements for any two Ising variable configurations, $\{s_l\}$ and $\{s'_l\}$;

$$g'(l,l') = g(l,l') + \sum_{l''} (g(l,l'') - \delta_{ll''})(e^{\lambda(s'_{l''} - s_{l''})} - 1) g'(l'',l'), \tag{B.6}$$

where g and g' are the matrix elements for two Ising variable configurations $\{s_l\}$ and $\{s'_l\}$, respectively. One of the most remarkable features of the algorithm is that the Monte Carlo samples $g(l,l')$ are produced by only the equation (B.6) of $g(l,l')$ themselves.

The Ising variable configurations are generated with a renewal probability $R(s_l \to s'_l)$. The renewal probability is also determined only by $g(l,l')$ themselves;

$$R(s_l \to s'_l) = 1 + (1 - g(l,l))(e^{\lambda(s'_l - s_l)} - 1). \tag{B.7}$$

Thus, we need not consider degree of freedom of the conduction electrons explicitly. Namely, if one only gives the expression of the bare Green's function

as an input of the procedure, one can calculate the full Green's function by the algorithm. The remarkable feature enables us to use the algorithm within the DMFT framework, because we have to calculate the local Green's function $G^d(\tau)$ only from $\mathcal{G}(\tau)$ in the DMFT.

B.1.2 Implementation of the quantum Monte Carlo method

In the results of the thesis, we show one-particle-excitation spectral functions only for the fixed value of L. This is because we have not found the distinctive differences in the spectral functions obtained by the maximum entropy method for the different values of L (see Fig. B.1. The parameters are as follows; $U_d = 5$, $\Delta = 3$, $\mu = -1.0$ and $\beta = 8$). In the practical calculations we set

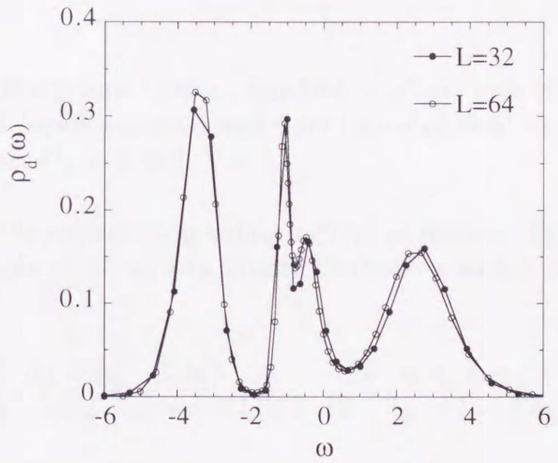

Figure B.1: L-dependence of the d-component spectrum for $L = 32$ (solid circles) and $L = 64$ (open circles).

$L = 64$ mainly.

In the Monte Carlo sampling procedure, we divide the samples into $N_{\rm bin}$ groups (bins), each of which has M samples, and measure the standard deviation among the $N_{\rm bin}$ bins. The measurement is usually carried out at every other Monte Carlo step in order to reduce the correlation between the samples. When the system is close to an insulating phase, the acceptance rate is small ($\lesssim 0.35$). In such a case we make the measurements at every 4 steps. Repeating the measurements, we collect $M = 4000 \sim 5000$ samples in a bin

and take $N_{\rm bin} = 200$ bins. That is, we take $8 \times 10^5 \sim 1 \times 10^6$ Monte Carlo samples.

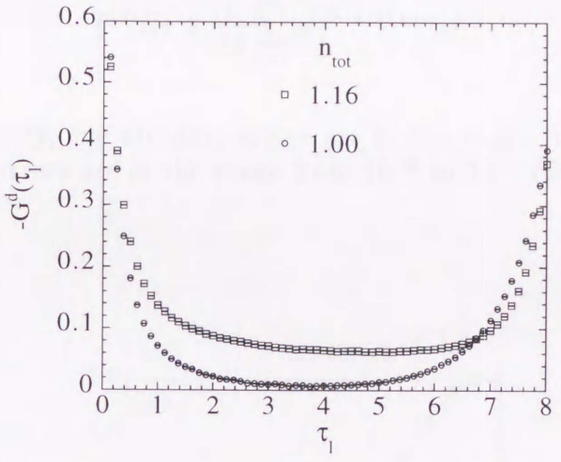

Figure B.2: Imaginary-time Green's function $-G^d(\tau_l)$ with the statistical error σ_l for $n_{\rm tot} = 1.16$ (open squares) and 1.00 (open circles) at $\beta = 8$ ($L = 64$). The parameters are $U_d = 5$ and $\Delta = 3$.

We calculate the expectation values $G^d(\tau_l)$ as follows. First, we define the Monte Carlo sample $g^{(i)}(l)$ at i-th Monte Carlo step with a random integer $l_{\rm R}$ ($1 \le l_{\rm R} \le L$),

$$g^{(i)}(l) \equiv \begin{cases} g(l + l_{\rm R} - 1, l_{\rm R}) & (\text{for } l_{\rm R} \le L - l + 1) \\ -g(l_{\rm R} - L + l - 1, l_{\rm R}) & (\text{for } l_{\rm R} > L - l + 1), \end{cases} \tag{B.8}$$

where $g(l, l')$ is the Green's function matrix element for a certain configuration of the Ising variables (see Section B.1.1). The random integer $l_{\rm R}$ is produced for any $g^{(i)}(l)$ at every Monte Carlo step. Second, we calculate $G^d(\tau_l)$ as the arithmetical mean values of $g^{(i)}(l)$,

$$G^d(\tau_l) \simeq \frac{1}{N_{\rm bin}} \sum_{k=1}^{N_{\rm bin}} \frac{1}{M} \sum_{i=1}^{M} g^{((k-1)M+i)}(l). \tag{B.9}$$

The statistical error σ_l for $G^d(\tau_l)$ is expressed as

$$\sigma_l^2 \equiv \frac{1}{N_{\rm bin}(N_{\rm bin} - 1)} \sum_{k=1}^{N_{\rm bin}} (\bar{g}^{(k)}(l) - G^d(\tau_l))^2, \tag{B.10}$$

where $\bar{g}^{(k)}(l)$ is defined as

$$\bar{g}^{(k)}(l) \equiv \frac{1}{M} \sum_{i=1}^{M} g^{((k-1)M+i)}(l). \tag{B.11}$$

In the present study, the absolute errors are in the range from 10^{-4} to 10^{-3} and the relative errors are in the range from 10^{-3} to 10^{-1} (Fig. B.2).

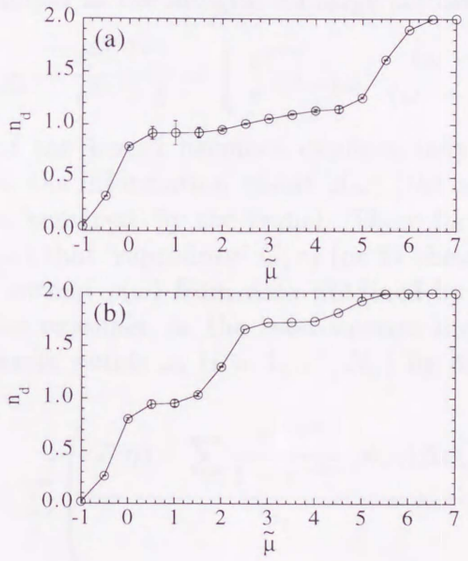

Figure B.3: Plots of the d-hole number density n_d with statistical errors for $(U_d, \Delta) =$ (a) $(5, 3)$ and (b) $(2.5, 4)$ at $\beta = 8$ $(L = 32)$.

The statistical errors in the $\mu - n$ plot are shown in Figs. B.3. It is shown that the error becomes larger near the insulating phase.

B.2 Maximum entropy method

B.2.1 Fundamental formulation

In order to obtain the one-particle-excitation spectral function $\rho(\omega)$ from $G(\tau_l)$, we have to carry out the analytic continuation. (Throughout this section, we omit the superscript d on ρ or G.) The analytic continuation problem is equivalent to the inversion of the transformation from $\rho(\omega)$ to $G(\tau)$;

$$G(\tau) = \int_{-\infty}^{\infty} \mathrm{d}\omega \rho(\omega) \frac{e^{-\tau\omega}}{1 + e^{-\beta\omega}}. \tag{B.12}$$

One calculates $G(\tau)$ by the quantum Monte Carlo simulation and obtains the data $\{G(\tau_l)\}$. Thus, they are subject to statistical errors. In eq.(B.12), the behavior of the kernel in the integral for large $|\omega|$ becomes as follows;

$$\frac{e^{-\tau\omega}}{1 + e^{-\beta\omega}} = \frac{e^{(\beta-\tau)\omega}}{e^{\beta\omega} + 1} \to \begin{cases} e^{-\tau\omega} & (\omega \to \infty) \\ e^{-(\beta-\tau)|\omega|} & (\omega \to -\infty) \end{cases}. \tag{B.13}$$

Namely, the value of the kernel becomes exponentially small for large $|\omega|$. Thus, in the integral, the information about $\rho(\omega)$ (the structure of the spectrum) for large $|\omega|$ is 'screened' by the kernel. These facts suggest that there exist innumerable $\rho(\omega)$ that 'reproduce' $G(\tau)$ (or fit the data). Therefore it is difficult to infer the correct $\rho(\omega)$ from data obtained by the quantum Monte Carlo simulation. For example, in the least-squares method, we obtain the optimal $\rho(\omega_i)$ at discrete points ω_i $(i = 1, \ldots, N_\omega)$ by minimizing χ^2 defined by

$$\chi^2 \equiv \sum_l \left(\frac{G(\tau_l) - \sum_i \frac{e^{-\tau_l\omega_i}}{1 + e^{-\beta\omega_i}} \rho(\omega_i) \Delta\omega_i}{\sigma_l} \right)^2, \tag{B.14}$$

where, σ_l is the statistical error of $G(\tau_l)$ and $\Delta\omega_i$ is the appropriate integration weight associated with a discrete frequency ω_i. In the method, however, the information about the positivity $(\rho(\omega_i) \geq 0)$ and the sum rule $(\sum_i \rho(\omega_i)\Delta\omega_i = 1)$ is not considered. Thus, there is a risk to obtain a non-physical $\rho(\omega_i)$. Namely, to minimize χ^2 is not always the best way to infer $\rho(\omega_i)$.

In the maximum entropy method [74, 75, 76], the information-theory entropy S is introduced to consider the positivity and the sum rule of $\rho(\omega_i)$. The entropy is defined as

$$S = \sum_i \left(\rho(\omega_i) - m(\omega_i) - \rho(\omega_i) \ln \frac{\rho(\omega_i)}{m(\omega_i)} \right) \Delta\omega_i, \tag{B.15}$$

where $m(\omega_i)$ is a default model. One gives a default model, which satisfies the positivity and the sum rule, as an input. The entropy is defined relative to the default model $m(\omega_i)$ for $\rho(\omega_i)$. If we are completely ignorant about $\rho(\omega_i)$ except for the positivity and sum rule before obtaining the Monte Carlo data, we take $m(\omega_i)$ to be flat in the frequency range of interest [76]. Since S take its maximum value, $S = 0$, at the case of $\rho(\omega_i) = m(\omega_i)$, we determine the optimal $\rho(\omega_i)$ by minimizing $\mathcal{F}$ defined by

$$\mathcal{F} \equiv \frac{\chi^2}{2} - \alpha S, \tag{B.16}$$

where χ^2 is defined by eq.(B.14) and α is a Lagrange multiplier determined from classic maximum entropy criterion [75, 76, 77] (see Section B.2.3). We can obtain the optimal $\rho(\omega_i)$ from the simultaneous equations,

$$\frac{\partial \mathcal{F}}{\partial \rho(\omega_i)} = 0 \quad (\text{for all } i). \tag{B.17}$$

B.2.2 Implementation of the maximum entropy method

We calculate the spectral function in the frequency region of interest; $\omega_{\min} \leq \omega \leq \omega_{\max}$. We discretize ω into ω_i $(i = 1, \ldots, N_\omega)$, where $\omega_1 = \omega_{\min}$, $\omega_{N_\omega} = \omega_{\max}$. To describe well the spectral function in the frequency region near the chemical potential μ, we use the discretization defined as follows;

$$\begin{aligned}
\omega_{N_- +1} &\equiv \mu, \\
\omega_{N_- -j+1} &\equiv \mu - C_- \frac{r^j - 1}{r - 1} \qquad (\text{for } \; 1 \leq j \leq N_-), \\
\omega_{N_- +j+1} &\equiv \mu + C_+ \frac{r^j - 1}{r - 1} \qquad (\text{for } \; 1 \leq j \leq N_+),
\end{aligned}$$

where N_+ and N_- are determined from $N_+ + N_- = N_\omega - 1$, $|(\omega_{\max} - \mu)/(\mu - \omega_{\min})| = N_+/N_-$. The coefficient C_+ and C_- are determined from $\omega_1 = \omega_{\min}$, $\omega_{N_\omega} = \omega_{\max}$. We choose $r = 1.1$. As for the $\omega_{\max}$, $\omega_{\min}$ and N_ω, we choose the value of them case by case. (For example, we take $N_\omega = 61$ for the $L = 64$ Monte Carlo data.)

In the practical procedure, we use the flat model as the default model, i.e. $m(\omega) = 1/(\omega_{\max} - \omega_{\min}) = \text{const.}$, because in the procedure of searching the solution we do not have any prior knowledges except for the positivity and the normalization of the spectral functions (see Section B.2.1). We have confirmed that there is few differences between the spectra obtained by using different

default models; the flat model which has no information and a "three peak" model which has a certain information such as the positions of the peaks (Fig. B.4). (In the "three peak" model, we assume that the spectrum is the (normalized) summation of three Gaussian spectra such as $e^{-(\omega-\omega^*)^2/(2\sigma^2)}/\sqrt{2\pi\sigma^2}$ with $(\omega^*, \sigma) = (-3.5, 1.0), (-0.5, 0.5), \text{and}(2.5, 1.0)$, respectively.)

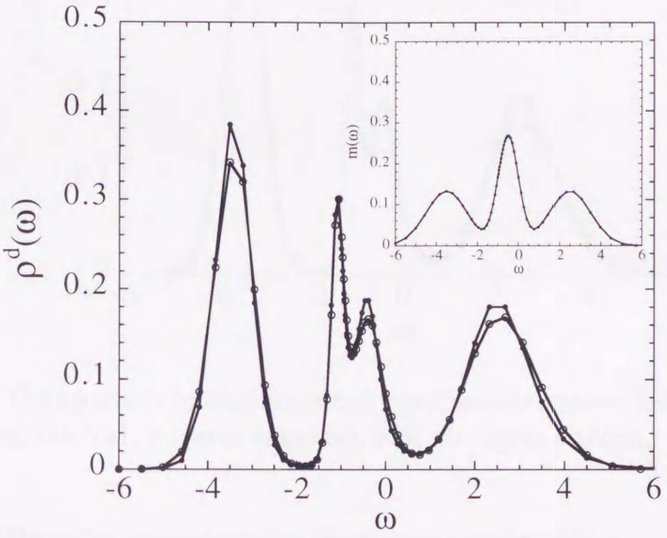

Figure B.4: Comparison of d-component spectra at $\beta = 8$ ($L = 64$) obtained from different default models; the flat model (solid circles) and the "three peak" model (open circles) which is shown in inset (see text). The parameters are $U_d = 5$ and $\Delta = 3$.

It is shown that (1) one can obtain the feature of the spectrum without any prior information except for the positivity and the sum rule, and (2) the formation of structures is not due to the prior information such as the position of the peak.

We use the classic maximum entropy criterion [74, 75, 76, 77] to determine the Lagrange multiplier α (see Section B.2.3). We have also confirmed that the spectrum is not so sensitive for the exact value of α (Fig. B.5).

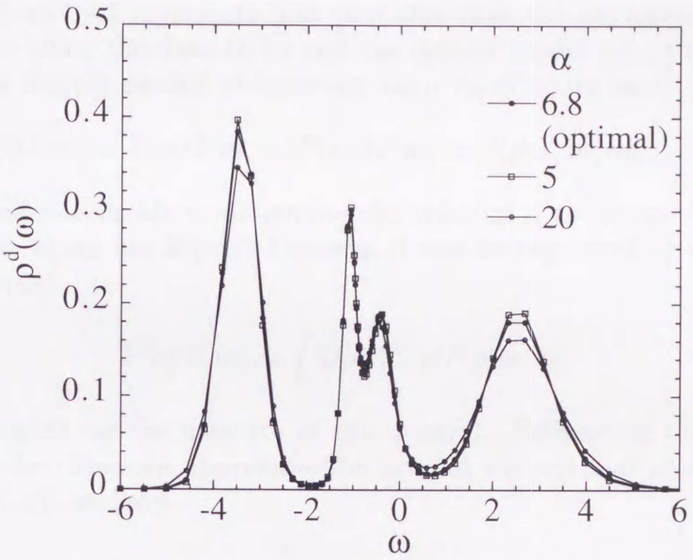

Figure B.5: Comparison of d-component spectra determined from different α: $\alpha = 6.8$ (solid circles), 5 (open squares), and 20 (open circles).

B.2.3 Classic maximum entropy criterion

From a Bayesian statistical point of view, the maximum entropy procedure is an inference process in which one searches for $\rho(\omega_i)$ that maximizes the conditional probability distribution function (PDF) $P[\rho|G,m]$. The PDF $P[\rho|G,m]$ shows how probable a certain form of $\rho(\omega_i)$ is when Monte Carlo data $G(\tau_l)$ and the default model $m(\omega_i)$ are given. Using Bayes's theorem, $P[\rho|G,m]$ can be written as

$$P[\rho|G,m] \propto P[G|\rho,m]P[\rho|m]. \tag{B.18}$$

The first term on the rhs is the likelihood function $P[G|\rho,m] \propto e^{-\chi^2/2}$. According to the information theory, it is known that $P[\rho|m]$ has the form,

$$P[\rho|m,\alpha] = \frac{e^{\alpha S}}{Z_S(\alpha)}, \tag{B.19}$$

where $Z_S(\alpha)$ is the normalization constant and $Z_S(\alpha) = (2\pi/\alpha)^{N_\omega/2}$ (N_ω is the number of the discrete points of ω_i).

To get the posterior PDF $P[\rho|G,m]$ we have to integrate out the parameter α,

$$P[\rho|G,m] = \int \mathrm{d}\alpha P[\rho|G,m,\alpha]P[\alpha|G,m]. \tag{B.20}$$

The PDF $P[\alpha|G,m]$ represents how probable that the parameter α takes a certain value when the data $G(\tau_l)$ and the default model $m(\omega_i)$ are given. If $P[\alpha|G,m]$ is sharply peaked at a certain value α_0 of α, we have

$$P[\rho|G,m] \simeq P[\rho|G,m,\alpha_0]P[\alpha_0|G,m] \propto P[\rho|G,m,\alpha_0]. \tag{B.21}$$

It is therefore reasonable to determine the value of α to be α_0. To calculate $P[\alpha|G,m]$ we again use Bayes's theorem; it can be expressed by the multiple integral of $\rho(\omega_i)$,

$$P[\alpha|G,m] \propto \int \mathrm{D}\rho P[G|\rho]P[\rho|m,\alpha], \tag{B.22}$$

where $\mathrm{D}\rho$ stands for the measure of the integral. Estimating the functional integral by the Gaussian approximation around the optimal $\rho(\omega_i)$ which we denote by $\hat{\rho}(\omega_i)$, we have

$$\begin{aligned} \ln P[\alpha|G,m] &\propto \ln \int \mathrm{D}\rho e^{\alpha S - \chi^2/2} - \ln Z_S(\alpha) + \text{const.} \\ &\propto \alpha S|_{\rho=\hat{\rho}} + \frac{1}{2}\sum_{i=1}^{N_\omega} \ln \frac{\alpha}{\alpha+\lambda_n} + \text{const.}, \end{aligned} \tag{B.23}$$

where λ_n are the eigenvalues of the Hessian matrix

$$\sqrt{\rho(\omega_i)}\frac{\partial^2(\chi^2/2)}{\partial\rho(\omega_i)\partial\rho(\omega_j)}\sqrt{\rho(\omega_j)}\bigg|_{\rho=\hat{\rho}}. \tag{B.24}$$

Thus, the optimal value α_0 of α is determined by

$$\frac{\partial \ln P[\alpha|G,m]}{\partial \ln \alpha}\bigg|_{\alpha=\alpha_0} = \alpha_0 S + \frac{1}{2}\sum_{i=1}^{N_\omega}\frac{\lambda_n}{\alpha_0+\lambda_n} = 0. \tag{B.25}$$

This is the classical maximum entropy criterion.

Appendix C

Exact diagonalization method within the DMFT framework

We show the procedure to solve the effective impurity problem in the DMFT framework using the exact diagonalization method [31] in this appendix.

As pointed out in Section 2.1.2, one can regard $\mathcal{G}(\mathrm{i}\omega_n)$ in the DMFT as a *bare* impurity Green's function of an impurity model. In the procedure, one approximates $\mathcal{G}(\mathrm{i}\omega_n)$ with a *bare* impurity Green's function $G^0_{\mathrm{And}}(\mathrm{i}\omega_n)$ of a finite-size cluster of an impurity Anderson model which is defined as follows;

$$\hat{\mathcal{H}}_{\mathrm{And}} = \varepsilon_0 \sum_{\sigma} d^\dagger_\sigma d_\sigma + \sum_{l=1,\sigma}^{N_s} \varepsilon_l c^\dagger_{l\sigma} c_{l\sigma} + \sum_{l=1,\sigma}^{N_s} V_l (d^\dagger_\sigma c_{l\sigma} + c^\dagger_{l\sigma} d_\sigma) + U d^\dagger_\uparrow d_\uparrow d^\dagger_\downarrow d_\downarrow. \quad \text{(C.1)}$$

The model consists of the 'impurity' level ε_0 and the levels ε_l $(l = 1, 2, \ldots, N_s)$ of the 'conduction electrons' hybridized with the impurity by V_l. The 'impurity' in eq.(C.1) corresponds to the local degree of freedom in the DMFT, respectively. The *free* Green's function of the d-electron is defined by

$$G^0_{\mathrm{And}}(\mathrm{i}\omega_n) = \frac{1}{\mathrm{i}\omega_n - \varepsilon_0 - \sum_{l=1}^{N_s} \dfrac{V_l^2}{\mathrm{i}\omega_n - \varepsilon_l}}. \quad \text{(C.2)}$$

We determine $2N_s + 1$ parameters $\{\varepsilon_0, \varepsilon_l, V_l (l = 1, 2, \ldots, N_s) | \varepsilon_1 < \varepsilon_2 < \cdots < \varepsilon_{N_s}\}$ by fitting $\mathcal{G}(\mathrm{i}\omega_n)$ with $G^0_{\mathrm{And}}(\mathrm{i}\omega_n)$, namely, by minimizing χ^2 with respect to the parameters. We define χ^2 as follows;

$$\chi^2 = \sum_{\mathrm{i}\omega_n} |(G^0_{\mathrm{And}}(\mathrm{i}\omega_n))^{-1} - (\mathcal{G}(\mathrm{i}\omega_n))^{-1}|^2. \quad \text{(C.3)}$$

After fitting, we diagonalize the finite cluster of the impurity Anderson model (C.1) with determined parameters, and calculate the N-particle eigenvectors $|\phi_{i_N}^{(N)}\rangle$ and corresponding eigenvalues $K_{i_N}^{(N)} \equiv E_{i_N}^{(N)} - \mu N$ of $\hat{\mathcal{H}}_{\rm And} - \mu\hat{N}$ in the (N_s+1)-site cluster. Note that $\hat{N} \equiv \sum_\sigma d_\sigma^\dagger d_\sigma + \sum_{l=1,\sigma}^{N_s} c_{l\sigma}^\dagger c_{l\sigma}$ is the number operator of the fictitious particles in the cluster of the impurity Anderson model, and it should not be confused with that of holes in the original lattice of the two-band Hubbard model. (Hereafter we refer to the cluster of the impurity Anderson model as the impurity Anderson cluster.)

By using the full set of states $|\phi_{i_N}^{(N)}\rangle$, we can calculate the local Green's function G^d,

$$G^d(\mathrm{i}\omega_n) = \frac{1}{\Xi}\sum_N \sum_{i_N j_N} |\langle\phi_{i_N}^{(N)}|d_\sigma^\dagger|\phi_{j_N}^{(N)}\rangle|^2 (\mathrm{e}^{-K_{i_N}^{(N)}} + \mathrm{e}^{-K_{j_N}^{(N)}}) \frac{1}{\mathrm{i}\omega_n - (K_{i_N}^{(N)} - K_{j_N}^{(N)})}, \tag{C.4}$$

where $\Xi \equiv \mathrm{Tr}\mathrm{e}^{-\beta\hat{K}}$. The Green's function is used to determine a new $\mathcal{G}$ iteratively. The iteration is continued until convergence is attained. Finally, we can obtain the Green's function in the spectral representation by the analytic continuations of $G^d(\mathrm{i}\omega_n)$ and $G^p(\mathrm{i}\omega_n)$.

Appendix D

Perturbative solution in single-cluster calculation

We summarize the property of the solutions for the single cluster of the two-band Hubbard model (3.11). For the Schrödinger equation (3.12), the one-particle ground state $|\Psi_{0\sigma}^{(1)}\rangle$ and the corresponding energy $E_0^{(1)}$ are expressed as follows;

$$|\Psi_{0\sigma}^{(1)}\rangle = a^d|d^1\rangle + a^p|p^1\rangle, \tag{D.1}$$

$$E_0^{(1)} = \frac{1}{2}(\varepsilon_p + \varepsilon_d - \sqrt{\Delta^2 + 4t^2}) \equiv \varepsilon_d + \delta_0^{(1)}, \tag{D.2}$$

where we define the energy gain $|\delta_0^{(1)}|$ ($\delta_0^{(1)} < 0$) of $|\Psi_{0\sigma}^{(1)}\rangle$ due to the hybridization with the p-level. The singlet states at $n_{\rm tot} = 2$ are expressed by

$$|\Psi_m^{(2)}\rangle = a_m^{dd}|d^2\rangle + a_m^{dp}|d^1p^1\rangle + a_m^{pp}|p^2\rangle. \tag{D.3}$$

The corresponding eigenvalues $E_m^{(2)}$ are determined by an eigenvalue equation,

$$(E_m^{(2)}-2\varepsilon_p)(E_m^{(2)}-(2\varepsilon_d+U))(E_m^{(2)}-(\varepsilon_p+\varepsilon_d))-2t^2(E_m^{(2)}-(2\varepsilon_d+U)+E_m^{(2)}-2\varepsilon_p) = 0. \tag{D.4}$$

For $U = 5$ and $\Delta = 3$, the values of coefficients of the one-particle ground state wave function are $|a^d|^2 = 0.92$ and $|a^p|^2 = 0.08$. We also show the coefficients of the singlet wave functions corresponding to the peaks of the result (Fig. 4.4(a)) by the QMC and ME methods in the table.

ω	$\lvert a^{dd}\rvert^2$	$\lvert a^{dp}\rvert^2$	$\lvert a^{pp}\rvert^2$
-0.8	0.15	0.76	0.09
2.7	0.72	0.05	0.23
4.1	0.12	0.20	0.68

The peak at $\omega = -0.8$ in Fig. 4.4(a) is caused by the transition to the d^1p^1 singlet state. We define the energy gain $|\delta_0^{(2)}|$ ($\delta_0^{(2)} < 0$) of the d^1p^1 state;

$$E_0^{(2)} = \varepsilon_p + \varepsilon_d + \delta_0^{(2)}. \tag{D.5}$$

Because this gain $|\delta_0^{(2)}|$ is larger than $|\delta_0^{(1)}|$, the spectrum line appears below $\omega = \varepsilon_p$, i.e., at $\omega = \varepsilon_p + \delta_0^{(2)} - \delta_0^{(1)} (< \varepsilon_p)$. (In the present result for $U = 5$ and $\Delta = 3$, $E_0^{(1)} = -3.3$ and $E_0^{(2)} = -4.1$.)

In the case with $U \gg \Delta \gg t$,

$$\delta_0^{(2)} = -2t^2\left(\frac{1}{U-\Delta} + \frac{1}{\Delta}\right), \tag{D.6}$$

$$\delta_0^{(1)} = -t^2\frac{1}{\Delta}, \tag{D.7}$$

and then

$$\delta_0^{(2)} - \delta_0^{(1)} = -2t^2\left(\frac{1}{U-\Delta} + \frac{1}{2\Delta}\right). \tag{D.8}$$

The difference $E_t^{(2)} - E_0^{(2)} = -\delta_0^{(2)}$ of the energy between the triplet state ($E_{\mathrm{t}}^{(2)} = \varepsilon_p + \varepsilon_d$) and the singlet state tends to be $2J_{\mathrm{K}}$, the exchange energy between a (localized) d-spin and a p-hole.

Appendix E

Spectral intensity at the Fermi level

We show that the spectral intensity at the Fermi level in the single-band Hubbard model is invariant as long as the system is the Fermi liquid state provided the self-energy is local [23], while that of the two-band Hubbard model decreases even though the self-energy is local. We follow Luttinger [78] to derive the above conclusions.

First, we consider the single-band Hubbard model. According the Luttinger's theorem, as long as the system satisfies the Fermi liquid condition ($\mathrm{Im}\Sigma(\omega)$ vanishes more rapidly than ω), the expression of the total number of particles N_{tot} using the Green's function can be rearranged in the absolute zero limit as follows;

$$
\begin{aligned}
N_{\mathrm{tot}} &= \sum_{\boldsymbol{k}\sigma} T \sum_{\mathrm{i}\omega_n} G_{\boldsymbol{k}}(\mathrm{i}\omega_n) e^{\mathrm{i}\omega_n \delta}|_{\delta\to 0+} && \text{(E.1)} \\
&= \sum_{\boldsymbol{k}\sigma} T \sum_{\mathrm{i}\omega_n} (\mathrm{i}\omega_n + \mu - \varepsilon_{\boldsymbol{k}} - \Sigma(\mathrm{i}\omega_n))^{-1} e^{\mathrm{i}\omega_n \delta}|_{\delta\to 0+} \\
&\to -\frac{1}{\pi} \sum_{\boldsymbol{k}\sigma} \mathrm{Im} \ln(\varepsilon_{\boldsymbol{k}} - \varepsilon_{\mathrm{F}} + \mathrm{Re}\Sigma(0) - \mathrm{i}\delta)|_{\delta\to 0+} \ (\text{as } T \to 0) \\
&= -\frac{1}{\pi} \sum_{\boldsymbol{k}\sigma} \arg(\varepsilon_{\boldsymbol{k}} - \varepsilon_{\mathrm{F}} + \mathrm{Re}\Sigma(0) - \mathrm{i}\delta)|_{\delta\to 0+} && \text{(E.2)} \\
&= \sum_{\boldsymbol{k}\sigma} \theta(\varepsilon_{\mathrm{F}} - \varepsilon_{\boldsymbol{k}} - \mathrm{Re}\Sigma(0)). \\
& && \text{(E.3)}
\end{aligned}
$$

The last expression implies that the Fermi surface determined by

$$\varepsilon_{\boldsymbol{k}} = \varepsilon_{\mathrm{F}} - \mathrm{Re}\Sigma(0), \tag{E.4}$$

and it does not change from that in the free ($U = 0$) case. (The Fermi surface in the free case is determined by $\varepsilon_{\boldsymbol{k}} = \varepsilon_{\mathrm{F}}^0$.) On the other hand, using the one-particle spectral function $\rho(\omega)$, N_{tot} is expressed by

$$N_{\mathrm{tot}} = N_L \sum_{\sigma} \int_{-\infty}^{0} \mathrm{d}\omega \rho(\omega), \tag{E.5}$$

where N_L is the number of sites. One can rearrange the expression (E.3) using the density of states $D(\epsilon) = \sum_{\boldsymbol{k}} \delta(\epsilon - \varepsilon_{\boldsymbol{k}})/N_L$ as

$$N_{\mathrm{tot}} = N_L \sum_{\sigma} \int_{-\infty}^{\infty} \mathrm{d}\epsilon D(\epsilon)\theta(\varepsilon_{\mathrm{F}} - \epsilon - \mathrm{Re}\Sigma(0)) \tag{E.6}$$

$$= N_L \sum_{\sigma} \int_{-\infty}^{0} \mathrm{d}\epsilon D(\epsilon + \varepsilon_{\mathrm{F}} - \mathrm{Re}\Sigma(0)). \tag{E.7}$$

One can obtain the value of the spectral intensity $\rho(0)$ at the Fermi surface by comparison of eq.(E.7) with eq.(E.5) as

$$\rho(0) = D(\varepsilon_{\mathrm{F}} - \mathrm{Re}\Sigma(0)). \tag{E.8}$$

On the other hand, the value of the spectral intensity $\rho_0(0)$ at the Fermi surface in the free case is expressed as $\rho_0(0) = D(\varepsilon_{\mathrm{F}}^0)$ Thus, it has been proved that the spectral intensity at the Fermi surface is invariant as long as the system is the Fermi liquid in the *single-band* Hubbard model with the $\boldsymbol{k}$-independent self-energy [23].

Let us carry out the similar procedure to treat the two-band Hubbard model. In the two-band Hubbard model, we should consider the matrix representation of the Green's function as

$$\hat{G}_{\boldsymbol{k}}(\mathrm{i}\omega_n) = \begin{pmatrix} \mathrm{i}\omega_n + \mu - \varepsilon_d - \Sigma(\mathrm{i}\omega_n) & -\nu_{\boldsymbol{k}} \\ -\nu_{\boldsymbol{k}} & \mathrm{i}\omega_n + \mu - \varepsilon_p \end{pmatrix}^{-1}, \tag{E.9}$$

where $\nu_{\boldsymbol{k}}$ is the Fourier transformation of the $d - p$ hybridization term of eq.(3.1) in 3.2. The rearrangement of the expression of the total number N_{tot} can be carried out in the similar way to the single-band case, and one obtains the expression corresponds to (E.2) at the absolute zero as follows;

$$N_{\mathrm{tot}} = -\frac{1}{\pi} \sum_{\boldsymbol{k}\sigma} \mathrm{Im}\,\mathrm{Tr}\,\ln \begin{pmatrix} \varepsilon_d - \varepsilon_{\mathrm{F}} + \mathrm{Re}\Sigma(0) - \mathrm{i}\delta & \nu_{\boldsymbol{k}} \\ \nu_{\boldsymbol{k}} & \varepsilon_p - \varepsilon_{\mathrm{F}} - \mathrm{i}\delta \end{pmatrix}\Bigg|_{\delta \to 0+}. \tag{E.10}$$

The expression corresponding to (E.3) can be obtained by diagonalizing the matrix in the natural logarithm in (E.10) as

$$N_{\rm tot} = \sum_{\boldsymbol{k}\sigma,\gamma=\pm} \theta(\varepsilon_{\rm F} - E^{\gamma}_{\boldsymbol{k}}), \tag{E.11}$$

where $E^{\gamma}_{\boldsymbol{k}}$ is the eigenvalue of the matrix in (E.10) and defined as

$$E^{\gamma}_{\boldsymbol{k}} \equiv \frac{1}{2}(\varepsilon_p + \tilde{\varepsilon}_d + \gamma\sqrt{\tilde{\Delta}^2 + 4\nu^2_{\boldsymbol{k}}}). \tag{E.12}$$

In the above expression, $\tilde{\varepsilon}_d$ and $\tilde{\Delta}$ are defined as $\tilde{\varepsilon}_d = \varepsilon_d + {\rm Re}\Sigma(0)$ and $\tilde{\Delta} = \Delta - {\rm Re}\Sigma(0)$, respectively.

One can obtain the similar expression to eq. (E.7) of the spectral intensity at the Fermi surface in the two-band Hubbard model as follows;

$$\sum_{\sigma,\gamma=\pm} \int_{-\infty}^{\infty} {\rm d}\nu D(\nu)\delta(\varepsilon_{\rm F} - E^{\gamma}(\nu)), \tag{E.13}$$

where we defined $E^{\gamma}(\nu_{\boldsymbol{k}}) \equiv E^{\gamma}_{\boldsymbol{k}}$. Hereafter, we assume that the Fermi level is in the lower band ($\gamma = -$) and consider the spectral intensity per spin. Thus, we take only $\gamma = -$ in the γ- summation and omit the spin summation in (E.13). By rearranging the δ-function in (E.13), the last expression of the spectral intensity at the Fermi surface can be obtained as follows;

$$\int_{-\infty}^{\infty} {\rm d}\nu D(\nu)\delta(\varepsilon_{\rm F} - E^{-}(\nu)) = \frac{\sqrt{\tilde{\Delta}^2 + 4(\varepsilon_{\rm F} - \varepsilon_p)(\varepsilon_{\rm F} - \tilde{\varepsilon}_d)}}{\sqrt{(\varepsilon_{\rm F} - \varepsilon_p)(\varepsilon_{\rm F} - \tilde{\varepsilon}_d)}} D(\sqrt{(\varepsilon_{\rm F} - \varepsilon_p)(\varepsilon_{\rm F} - \tilde{\varepsilon}_d)}). \tag{E.14}$$

On the other hand, according to the expression (E.11), the Fermi surfaces in the free case and the interacting case are determined by $\varepsilon_{\rm F} - E^{-}(\nu) = 0$ and $\varepsilon^0_{\rm F} - E^{-}_0(\nu) = 0$, respectively. ($E^{\gamma}_0(\nu)$ is the dispersion in the free case.) Namely, the relation which is satisfied by $\varepsilon_{\rm F}$ and ${\rm Re}\Sigma(0)$ is expressed by

$$(\varepsilon_{\rm F} - \varepsilon_p)(\varepsilon_{\rm F} - \tilde{\varepsilon}_d) = (\varepsilon^0_{\rm F} - \varepsilon_p)(\varepsilon^0_{\rm F} - \varepsilon_d). \tag{E.15}$$

Using the relation, we can finally estimate the spectral intensity at the Fermi surface for small ${\rm Re}\Sigma(0)$ in the interacting case as follows;

$$\int_{-\infty}^{\infty} {\rm d}\nu D(\nu)\delta(\varepsilon_{\rm F} - E^{-}(\nu)) \tag{E.16}$$

$$\simeq \frac{\sqrt{\Delta^2 + 4(\varepsilon^0_{\rm F} - \varepsilon_p)(\varepsilon^0_{\rm F} - \varepsilon_d)}}{\sqrt{(\varepsilon^0_{\rm F} - \varepsilon_p)(\varepsilon^0_{\rm F} - \varepsilon_d)}} D(\sqrt{(\varepsilon^0_{\rm F} - \varepsilon_p)(\varepsilon^0_{\rm F} - \varepsilon_d)})(1 - \frac{{\rm Re}\Sigma(0)\Delta}{\Delta^2 + 4(\varepsilon^0_{\rm F} - \varepsilon_p)(\varepsilon^0_{\rm F} - \varepsilon_d)}),$$

where we assume $\Delta \gg \mathrm{Re}\Sigma(0)$. It implies that the spectral intensity at the Fermi surface of the two-band Hubbard model with the $\boldsymbol{k}$-independent self-energy in the interacting case is smaller than that in the free case as long as $\mathrm{Re}\Sigma(0) > 0$, because the term $(\varepsilon_{\mathrm{F}}^0 - \varepsilon_p)(\varepsilon_{\mathrm{F}}^0 - \varepsilon_d)$ is always positive.

Bibliography

[1] J.G. Bednorz and K.A. Müller, Z. Phys. **B64** (1986) 189.

[2] J. Zaanen, G.A. Sawatzky, and J.W. Allen, Phys. Rev. Lett. **55** (1985) 418; J. Zaanen and G.A. Sawatzky, Can. J. Phys. **65** (1987) 1262.

[3] J.H. de Boer and E.J.W. Verwey, Proc. Phys. Soc. (London) **49** (1937) 59.

[4] N.F. Mott and R. Peierls, Proc. Phys. Soc. (London) **49** (1937) 72.

[5] N.F. Mott, Proc. Phys. Soc. (London) **A62** (1949) 416.

[6] N.F. Mott, Phil. Mag. **6** (1961) 287.

[7] H. Takagi, T.Ido, S. Ishibashi, M. Uota, S. Ueda, and Y. Tokura, Phys. Rev. **B40** (1989) 2254.

[8] J.B. Torrance, Y. Tokura, A.I. Nazzal, A. Bezinge, T.C. Huang, S.S.P. Parkin, Phys. Rev. Lett. **61** (1988) 1127.

[9] J.B. Torrance, A. Bezinge, A.I. Nazzal, T.C. Huang, S.S.P. Parkin, D.T. Keane, S.J. LaPlaca, P.M. Horn, and G.A. Held, Phys. Rev. **B40** (1989) 8872.

[10] J. Hubbard, Proc. Roy. Soc. (London) **A276** (1963) 238.

[11] J. Hubbard, Proc. Roy. Soc. (London) **A281** (1964) 401.

[12] D.M. Edwards and A.C. Hewson, Rev. Mod. Phys. **40** (1968) 810.

[13] W.F. Brinkman and T.M. Rice, Phys. Rev. **B2** (1970) 4302.

[14] M.C. Gutzwiller, Phys. Rev. Lett. **10** (1963) 159; M.C. Gutzwiller, Phys. Rev. **134** (1964) A923; M.C. Gutzwiller, Phys. Rev. **137** (1965) A1726.

[15] H. Yokoyama and H. Shiba, J. Phys. Soc. Jpn. **56** (1987) 1490.

[16] For a recent review, see D. Vollhardt, in *Correlated Electron Systems*, edited by V.J. Emery (World Scientific,Singapore, 1992), p.57; A. Georges, G. Kotliar, W. Krauth, and M.J. Rozenberg, Rev. Mod. Phys. **68** (1996) 13.

[17] A. Georges and G. Kotliar, Phys. Rev. B**45** (1992) 6479.

[18] X.Y. Zhang, M.J. Rozenberg, and G. Kotliar, Phys. Rev. Lett. **70** (1993) 1666.

[19] A. Georges and W. Krauth, Phys. Rev. B**48** (1993) 7167.

[20] E.H. Lieb and F.Y. Wu, Phys. Rev. Lett. **20** (1968) 1445.

[21] W. Metzner and D. Vollhardt, Phys. Rev. Lett. **62** (1989) 324.

[22] E. Müller-Hartmann, Z. Phys. B**74** (1989) 507.

[23] E. Müller-Hartmann, Z. Phys. B**76** (1989) 211.

[24] M. Jarrell, Phys. Rev. Lett. **69** (1992) 168.

[25] M. Jarrell and Th. Pruschke, Z. Phys. B**90** (1993) 187.

[26] K. Wilson, Rev. Mod. Phys. **47** (1975) 773.

[27] K. Yamada, Prog. Theor. Phys. **53** (1975) 970; K. Yosida and K. Yamada, Prog. Theor. Phys. **53** (1975) 1286.

[28] J.E. Hirsch and R.M. Fye, Phys. Rev. Lett. **56** (1986) 2521.

[29] H. Kajueter and G. Kotliar, Phys. Rev. Lett. **77** (1996) 131.

[30] O. Sakai and Y. Kuramoto, Solid State Commun. **89** (1994) 307.

[31] M. Caffarel and W. Krauth, Phys. Rev. Lett. **72** (1994) 1545.

[32] M.J. Rozenberg, X.Y. Zhang, and G. Kotliar, Phys. Rev. Lett. **69** (1992) 1236.

[33] A. Georges and W. Krauth, Phys. Rev. Lett. **69** (1992) 1240.

[34] T. Saso and T. Hayashi, J. Phys. Soc. Jpn. **63** (1994) 401.

[35] T. Saso and A. Oguri, Physica B**206**&**207** (1995) 174.

[36] A. Fujimori, F. Minami, and S. Sugano, Phys. Rev. B**29** (1984) 5225; A. Fujimori and F. Minami, Phys. Rev. B**30** (1984) 957.

[37] G.A. Sawatzky and J.W. Allen, Phys. Rev. Lett. **53** (1984) 2339.

[38] A. Georges, G. Kotliar, and W. Krauth, Z. Phys. B**92** (1993) 313.

[39] H. Eskes and G.A. Sawatzky, Phys. Rev. Lett. **61** (1988) 1415.

[40] A. Fujimori, Phys. Rev. B**39** (1989) 793.

[41] A. Fujimori, in "*Strong Correlation and Superconductivity* " edited by H. Fukuyama, S. Maekawa, and A.P. Malozemoff (Springer-Verlag, Berlin, 1989), p.300.

[42] A. Fujimori, E. Takayama-Muromachi, and Y. Uchida, Solid State Commun. **63** (1987) 857.

[43] A. Bianconi, *et al.*, Solid State Commun. **63** (1987) 1009.

[44] Zhi-xun Shen, *et al.*, Phys. Rev. B**36** (1987) 8414.

[45] N. Nücker, J. Fink, J.C. Fuggle, P.J. Durham, and W.M. Temmerman, Phys. Rev. B**37** (1988) 5158.

[46] J. Fink, N. Nücker, H. Romberg, M. Alexander, G. Roth, and P. Adelmann, in "*Electronic Properties of High-T_c Superconductors and Related Compounds*" edited by H. Kuzmany, M. Mehring, and J. Fink (Springer-Verlag, Berlin, 1990), p.100.

[47] H. Romberg, M. Alexander, N. Nücker, P. Adelmann, and J. Fink, Phys. Rev. B**42** (1990) 8768.

[48] C.T. Chen, *et al.*, Phys. Rev. Lett. **66** (1991) 104.

[49] H. Romberg, M. Alexander, N. Nücker, P. Adelmann, and J. Fink, in "*Electronic Properties of High-T_c Superconductors and Related Compounds*" edited by H. Kuzmany, M. Mehring, and J. Fink (Springer-Verlag, Berlin, 1990), p.172.

[50] C.M. Varma, S. Schmitt-Rink, and E. Abrahams, Solid State Commun. **62** (1987) 681.

[51] V.J. Emery, Phys. Rev. Lett. **58** (1987) 2794.

[52] H. Matsumoto, M. Sasaki, and M. Tachiki, Solid State Commun. **71** (1989) 829.

[53] H. Jichu, T. Matsuura, and Y. Kuroda, J. Phys. Soc. Jpn. **58** (1989) 4280; H. Jichu, T. Matsuura, and Y. Kuroda, J. Phys. Soc. Jpn. **59** (1990) 2820.

[54] T. Matsuura, K. Miura, Y. Ōno, D. Hirashima, and Y. Kuroda, Prog. Theor. Phys. Suppl. No.106 (1991) 51.

[55] C.A.R. Sá de Melo and S. Doniach, Phys. Rev. B**41** (1990) 6633.

[56] J. Wagner, W. Hanke, and D. J. Scalapino, Phys. Rev. B**43** (1991) 10517.

[57] T. Tohyama and S. Maekawa, Physica C **185-189** (1991) 1575; T. Tohyama and S. Maekawa, Physica C **191** (1992) 193.

[58] T. Mutou, H. Takahashi, and D.S. Hirashima, unpublished.

[59] M. Sera, S. Shamoto, and M. Sato, Solid State Commun. **72** (1989) 749.

[60] A. Iwai, M. Abe, H. Nakajima, and K. Kumagai, Physica C **185-189** (1991) 1349.

[61] N. Wada, T. Obana, Y. Nakamura, and K. Kumagai, Physica B **165&166** (1990) 1341.

[62] A. Fujimori, Y. Tokura, H. Eisaki, H. Takagi, S. Uchida, and M. Sato, Phys. Rev. B**40** (1989) 7303.

[63] F.C. Zhang and T.M. Rice, Phys. Rev. B**37** (1988) 3759.

[64] A. Fujimori, I. Hase, M. Nakamura, H. Namatame, Y. Fujishima, Y. Tokura, M. Abbate, F.M.F. de Groot, M.T. Czyzyk, J.C. Fuggle, O. Strebel, F. Lopez, M. Domke, and G. Kaindl, Phys. Rev. B**46** (1992) 9841.

[65] I.H. Inoue, I. Hase, Y. Aiura, A. Fujimori, Y. Haruyama, T. Maruyama, Y. Nishihara, Phys. Rev. Lett. **74** (1995) 2539.

[66] I.H. Inoue, K. Morikawa, H. Fukuchi, T. Tsuji, F. Iga, and Y. Nishihara, Jpn. J. Appl. Phys. **32** (1993) 451.

[67] A. Fukushima, F. Iga, I.H. Inoue, K. Murata, and Y. Nishihara, J. Phys. Soc. Jpn. **63** (1994) 409.

[68] M. Onoda, H. Ohta, and H. Nagasawa, Solid State Commun. **79** (1991) 281.

[69] D. Hirashima and T. Mutou, in "*Research Report on Anormalous Metallic State near the Mott Transition*" edited by H. Fukuyama and A. Fujimori (Scientific Research in Priority Areas No.258 Ministry of Education Science, Sports and Culture, 1996), p.28.

[70] I.H. Inoue, H. Makino, I. Hase, M. Ishikawa, N.E. Hussey, and M.J. Rozenberg, to be published.

[71] I.H. Inoue, in Proceedings of Physical Phenomena at High Magnetic Fields II, May 1995 (Tallahassee, USA).

[72] D.D. Sarma, S.R. Barman, H. Kajueter, and G. Kotliar, Physica B **223&224** (1996) 496.

[73] H. Kajueter, G. Kotliar, D.D. Sarma, and S.R. Barman, preprint.

[74] S.F. Gull: in *Maximun-Entropy and Beyesian Methods in Science and Engineering*, edited by G.J. Erickson and C.R. Smith (Kluwer Academic, Dordrecht, 1988), p. 53; J. Skilling: in *Maximum Entropy and Beyesian Methods*, edited by J. Skilling (Kluwer Academic, Dordrecht, 1989), p. 45; S.F. Gull: *ibid.*, p.53.

[75] R.N. Silver, D.S. Sivia, and J.E. Gubernatis, Phys. Rev. B**41** (1990) 2380.

[76] J.E. Gubernatis, M. Jarrell, R.N. Silver, and D.S. Sivia, Phys. Rev. B**44** (1991) 6011.

[77] T. Mutou and D.S. Hirashima, J. Phys. Soc. Jpn. **64** (1995) 4799.

[78] J.M. Luttinger and J.C. Ward, Phys. Rev. **118** (1960) 1417; J.M. Luttinger, Phys. Rev. **119** (1960) 1153.

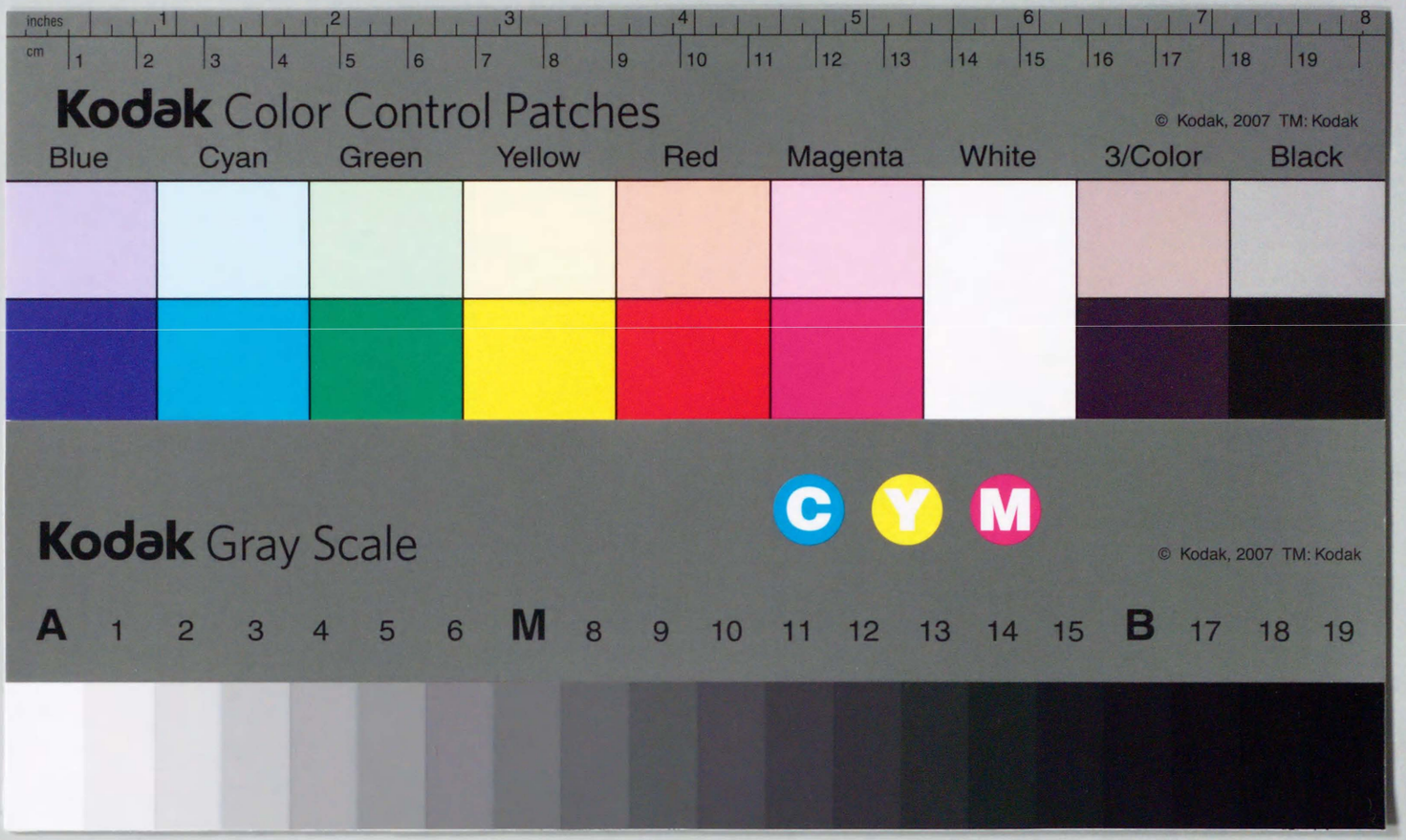
inches
cm
Kodak Color Control Patches
© Kodak, 2007 TM: Kodak
Blue
Cyan
Green
Yellow
Red
Magenta
White
3/Color
Black
Kodak Gray Scale
C
Y
M
© Kodak, 2007 TM: Kodak
A 1 2 3 4 5 6 M 8 9 10 11 12 13 14 15 B 17 18 19